Precise probing and discrimination of third-generation scalar leptoquarks

Anupam Ghosh,[1,2,*] Partha Konar,[1,†] Debashis Saha,[1,‡] and Satyajit Seth[1,§]

[1]*Theoretical Physics Division, Physical Research Laboratory, Shree Pannalal Patel Marg, Ahmedabad, 380009, Gujarat, India*

[2]*Discipline of Physics, Indian Institute of Technology, Palaj, Gandhinagar, 382424, Gujarat, India*

(Received 13 June 2023; accepted 3 July 2023; published 22 August 2023)

We explore the pair production of third-generation scalar leptoquark at the Large Hadron Collider to next-to-leading order accuracy in QCD, matched to parton shower for a precise probing of the stemming model. We propose to tag two boosted toplike fatjets produced from the decay of heavy leptoquarks in association with notably large missing transverse momentum and consider them as the potential signal. Such a signal demonstrates the capability of a robust discovery prospect in the multivariate analysis with different high-level observables, including jet substructure variables. Various scalar leptoquark models predict different chirality of the top quark appearing from the decay of the leptoquark carrying the same electromagnetic charge. We make use of the polarization variables sensitive to the top-quark polarization in order to identify the underlying theory.

DOI: 10.1103/PhysRevD.108.035030

I. INTRODUCTION

Leptoquark (LQ) is a hypothetical particle that couples to quark and lepton together. It carries both baryon number and lepton number and provides a means to unify quarks and leptons. It can appear in many interesting scenarios beyond the Standard Model, for example, Pati-Salam model [1,2], grand unified theory [3,4], composite model [5], etc., and therefore it remains a very active area in experimental searches. In some of these models, the baryon number gets violated and that allows protons to decay. But, the strong constraints from the nonobservation of proton decay so far have pushed the masses of the leptoquark to a very high scale, typically around 10^{16} GeV. However, imposing baryon number or lepton number conservation one gets a set of leptoquarks in the Buchmüller-Rückl-Wyler framework [6], which allows leptoquark masses to be in a range accessible to the collider searches. Also, such leptoquarks are favorable to explain anomalies observed in the B-meson decays in *BABAR* [7], Belle [8–10], and LHCb experiments [11,12]. Note that recent results from the LHCb with 9 fb^{-1} of data have made the anomaly disappear in the measurement of neutral current observables, i.e., R_K and R_{K^*}[1] [13,14]. Although these new results imply no lepton flavor universality violation in the flavor-changing neutral current from the decay of B meson, they do not exclude the possibility of the existence of a TeV-scale leptoquark. Such results only indicate that if a TeV-scale leptoquark exists, either it may not couple to the bottom and strange quarks at the same time together with a lepton, or the couplings are such that they get canceled in the ratio of the decay widths. Further implications of the LHCb results on the parameter space of different leptoquark models in various production channels have been discussed in [15].

In low-energy experiments, leptoquarks may be probed indirectly because they appear as off-shell states. Here, optimal ratios are formed to reduce the uncertainty due to hadronic activities. However, the number of theory parameters that enter through such ratios also increases. Instead, in the present and future high-energy collider experiments, leptoquarks can be searched directly and indirectly looking into a specific production channel. In order to explain the observation of anomaly, the leptoquark is needed to be coupled to fermions of different generations, in addition to the same generation quark and lepton. Although in most of the previous direct searches leptoquark couplings were considered generationwise, recent experimental studies are extended to include different cross-generation fermions [16,17]. Bounds on the first and second-generation scalar leptoquarks are obtained at the LHC considering production of either two charged light leptons of the same flavor or one charged light lepton with sizable missing transverse

*anupam@prl.res.in
†konar@prl.res.in
‡debasaha@prl.res.in
§seth@prl.res.in

[1] $R_K = \frac{\Gamma(B\to K\mu^+\mu^-)}{\Gamma(B\to Ke^+e^-)}$ and $R_{K^*} = \frac{\Gamma(B\to K^*\mu^+\mu^-)}{\Gamma(B\to K^*e^+e^-)}$.

energy together with a pair of jets. The limits on the parameters of the different components of the leptoquark model are obtained assuming different branching fractions. At 95% CL, ATLAS Collaboration has constrained the mass of first two-generation scalar leptoquarks up to 1400 GeV assuming 100% branching into certain decay modes with 36.1-fb^{-1} data [18]. The CMS Collaboration has also excluded masses below 1430 and 1530 GeV for the first and second generation, respectively, with 35.9-fb^{-1} data using the same branching fraction [19,20]. For the recent bounds on the vector leptoquark from collider searches, see Refs. [21–23].

In this work, we focus on the third-generation scalar leptoquarks. Phenomenology of such leptoquarks is studied widely in different channels [24–27] and they are also searched by the ATLAS and CMS Collaborations [21,22,28,29]. In a recent analysis [30], the ATLAS Collaboration did a cut-based analysis and extracted the limit for the up-type third-generation scalar leptoquark, assuming LQ decaying into a top quark and neutrino with a 100% branching ratio. Their analysis put a lower limit of 1240 GeV on the LQ mass at 95% CL for an integrated luminosity of 139 fb^{-1} at the 13-TeV LHC. This paper presents an alternative search strategy considering two toplike fatjets plus significant missing energy in the final state with a sophisticated multivariate analysis of the next-to-leading order plus parton shower (NLO + PS) signal events including jet substructure variables. Given the already-constrained parameter space, a relatively heavy leptoquark would naturally produce top quark at the boosted region once produced from its decay. Thus, it is prudent to identify such top quarks as a toplike fatjet from its hadronic decay. Note that the corresponding leptonic decay mode not only suffers from branching ratio suppression, but also identifying such leptons inside a jetty signature is a challenging task and therefore it affects the efficiency significantly. We observe that our result is consistent with the existing search and find that the third-generation LQ can be discovered with a significance of $\geq 5\sigma$ for masses below 1380 GeV with 3000-fb^{-1} data at the High-Luminosity LHC (HL-LHC).

Further, we put limit on the LQ mass up to which HL-LHC can exclude such LQ models with 95% confidence level. For the third-generation leptoquark, $t\bar{t}$ plus missing energy channel was also used in Ref. [31], where the authors found that $Z+$ jets is the main background, while $t\bar{t}+$ jets is the negligible one. However, the monoboson background can be controlled substantially by enforcing at least one b tagging inside the leading or subleading toplike fatjet. Such a demand in our analysis brings the monoboson background into a similar footing as $t\bar{t}+$ jets, thereby improving the result significantly.

Once discovered, the next goal would be distinguishing scalar leptoquarks of the same electromagnetic charge. Therefore, we also analyze distinguishing different scalar leptoquark models based on the same final-state signature at the LHC. One proposal has been made to determine different leptoquark types of the same spin and different electromagnetic charges by measuring jet charge [32]. We show that in the context of third-generation up-type leptoquark, measuring the polarization of the top quark resulting from the leptoquark decay can be an efficient way to distinguish scalar leptoquark models of the same electromagnetic charge without requiring the measurement of jet charge. In this work, for the first time, we use polarization variables to distinguish two scalar leptoquark models, considering all the backgrounds.

As the top quark decays before it hadronizes, its spin information can be obtained from its decay products[2] [33]. Top-quark polarization has been studied for more than the last 30 yr [34–46]. Determination of the polarization of boosted top quark is studied in [47]. The possibility of distinguishing two models in the $t\bar{t}\tau\bar{\tau}$ channel was explored before for scalar leptoquark in Ref. [48] without signal-to-background study. The prospect of distinguishing a scalar leptoquark from the background based on polarization variables at the LHC was shown to be small [49]. The potential of discriminating two specific beyond the standard model (BSM) scenarios in monotop search at the LHC using top polarization has been explored in [50].

We set our probe strategy based on two chosen leptoquark models, namely S_3 and R_2, that produce same pair-production cross section, but the top quark is produced as left and right chiral for these models, respectively. We find the difference in the kinematic distributions of these two models due to different chirality rendering minimal effect in separating the signal from the background. It leads to the almost identical mass limit for exclusion and discovery potential of these two models. However, one can use the polarization variables like the ratio of the b-jet energy to the reconstructed top-jet energy to distinguish two models at 14-TeV LHC and a futuristic 27-TeV collider (HE-LHC).

We consider the signal events at the NLO in QCD matched to PS for reduced-scale uncertainties and realistic results. By matching the fixed-order (FO) NLO correction with the PS [51,52], we get more accurate results for different kinematic distributions as it resums large leading logarithms in the collinear region. We show the effect of NLO + PS calculations on different kinematic distributions of the leptoquarks.

The rest of the paper is organized as follows. In Sec. II, we describe the third-generation scalar leptoquark models. In Sec. III, we show the effect of NLO calculations. We study the impact of parton shower over the FO NLO calculation, k-factor variation in differential distributions, and reduction of scale uncertainties at the NLO + PS accuracy. In Sec. IV, we describe our search strategy and provide details on multivariate analysis used to discriminate the signal and the background. In Sec. V, we discuss how

[2]Other quarks form bound states before their decay and hence lose their spin information.

TABLE I. All the possible scalar leptoquark models which give gauge-invariant terms in the Lagrangian under the SM gauge group transformations. To learn about the naming convention used for the models, see the text.

Models	$(SU(3)_c, SU(2)_L, U(1)_Y)$	Components and decay
S_3	$(\bar{3}, 3, \frac{1}{3})$	$S_3^{\frac{4}{3}}(\tilde{b}, \tau^+), S_3^{\frac{1}{3}}((\tilde{t}, \tau^+), (\tilde{b}, \tilde{\nu}_\tau)), S_3^{-\frac{2}{3}}(\tilde{t}, \tilde{\nu}_\tau)$
R_2	$(3, 2, \frac{7}{6})$	$R_2^{\frac{5}{3}}(t, \tau^+), R_2^{\frac{2}{3}}((t, \tilde{\nu}_\tau), (b, \tau^+))$
$\tilde{R}_2$	$(3, 2, \frac{1}{6})$	$\tilde{R}_2^{\frac{2}{3}}((t, \tilde{N}_\tau), (b, \tau^+)), \tilde{R}_2^{-\frac{1}{3}}((b, \tilde{\nu}_\tau), (b, \tilde{N}_\tau))$
$\tilde{S}_1$	$(\bar{3}, 1, \frac{4}{3})$	$\tilde{S}_1^{\frac{4}{3}}(\tilde{b}, \tau^+)$
S_1	$(\bar{3}, 1, \frac{1}{3})$	$S_1^{\frac{1}{3}}((\tilde{t}, \tau^+), (\tilde{b}, \tilde{\nu}_\tau), (\tilde{b}, \tilde{N}_\tau))$
$\bar{S}_1$	$(\bar{3}, 1, -\frac{2}{3})$	$\bar{S}_1^{-\frac{2}{3}}(\tilde{t}, \tilde{N}_\tau)$

the polarization observables can be instrumental in distinguishing two above-mentioned models. Finally, we summarize and conclude in Sec. VI.

II. THE MODELS

Under the Standard Model (SM) gauge group $SU(3)_c \otimes SU(2)_L \otimes U(1)_Y$, there are total six species of scalar leptoquarks, namely S_3, R_2, $\tilde{R}_2$, $\tilde{S}_1$, S_1, and $\bar{S}_1$. Since a quark transforms as a triplet of $SU(3)_c$, a leptoquark should also transform as the same multiplet of $SU(3)_c$ in order to form gauge-invariant interaction terms. In Table I, we show the SM quantum numbers of all scalar leptoquarks. The subscripts on the model name denote their $SU(2)_L$ quantum numbers. If two or more models have the same $SU(2)_L$ quantum number but different hypercharges, a tilde or bar is used to identify them. The component fields of the electroweak multiplets are written in the third column of the table with superscripts denoting their electric charges. In this article we are interested in studying the third-generation scalar leptoquarks only. Various decay channels of the component fields for third-generation leptoquarks are written inside parentheses.

It is interesting to notice that in only two models fields transform as **3** and for the rest of the models they transform as $\bar{\mathbf{3}}$ under $SU(3)_c$. Let us, for example, consider the S_3 model in which fields transform as $\bar{\mathbf{3}}$. The reason behind this transformation is that the fields in S_3 should couple to a quark doublet Q and lepton doublet L, as it transforms as **3** under $SU(2)_L$.[3] But, it can couple to only $\overline{Q^C}L$, not with $\overline{Q}L$, since the latter is zero. As $\overline{Q^C}$ transforms as **3**, S_3 would transform as $\bar{\mathbf{3}}$.[4] Obviously the conjugate of S_3 transforms as **3**, however, for that lepton doublet precedes the quark doublet in the Lagrangian. Here, we label a leptoquark as field (as opposed to the conjugate field) if in the interaction term quark precedes lepton. Transformation properties of the other leptoquarks under $SU(3)_c$ can be understood in a similar way.

One might be interested to probe third-generation up-type scalar leptoquark component fields which have $\frac{2}{3}e$ electric charge. There are four such component fields, namely $S_3^{-\frac{2}{3}}$, $R_2^{\frac{2}{3}}$, $\tilde{R}_2^{\frac{2}{3}}$, and $\bar{S}_1^{-\frac{2}{3}}$. At the LHC, the first two fields can give two top fatjets plus missing energy as the signature, whereas the last two, depending on the right-handed heavy neutrino decay mechanisms, will give more complicated and model-dependent signatures. In this paper, we are interested to study the phenomenology of the $S_3^{-\frac{2}{3}}$ and $R_2^{\frac{2}{3}}$ fields only.

The kinetic term for the generic scalar leptoquark (S) can be written as

$$\mathcal{L}_{\text{kin}} = (D_\mu S)^\dagger (D^\mu S) - M_S^2 S^\dagger S. \tag{2.1}$$

Here, the covariant derivative D_μ is given as

$$D_\mu = \partial_\mu - i g_s \lambda^a G_\mu^a, \tag{2.2}$$

where g_s is the strong coupling; λ^a and G^a $(a = 1, \ldots, 8)$ denote the Gellman matrices and gluon fields, respectively. The above Lagrangian gives rise to the following two vertices: (i) gluon-LQ-LQ, and (ii) gluon-gluon-LQ-LQ. The Feynman rules for these vertices are independent of the type of leptoquarks.

The quantum numbers of leptoquark S_3 are such that it can allow diquark coupling. However, without baryon or lepton number conservation, for TeV-scale leptoquark, this coupling has to be too tiny as otherwise it would lead to proton decay.[5] As this coupling is too constrained,

[3] $2 \otimes 2 = 3 \oplus 1$.

[4] For R_2 model, fields transform as **2** under $SU(2)_L$ and therefore one fermion needs to be doublet, while the other one needs to be singlet. The doublet and singlet are left- and right-handed, respectively. Hence, in this case, interaction with charge-conjugated quark field vanishes, while the one without charge conjugation survives. This explains why R_2 transforms as **3** under $SU(3)_c$.

[5] The models R_2 and $\tilde{R}_2$ which do not allow any diquark coupling are called genuine leptoquark. The other four scalar leptoquark models allow diquark couplings.

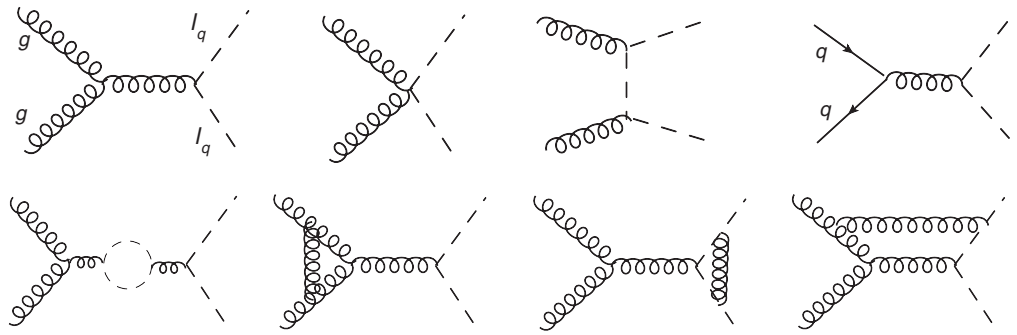

FIG. 1. In the upper row, all possible prototype born diagrams are shown. In the lower row, only a few prototype virtual diagrams are shown.

in our analysis they do not play any role.[6] The interaction terms for the third-generation scalar leptoquarks S_3 and R_2 of charge $\frac{2}{3}e$, with a quark and a lepton, are given by [53]

$$\mathcal{L}_{\rm Int}^{S_3^{\frac{2}{3}}} = y_{S_{LL}} * \overline{t_L^C} v_\tau S_3^{-\frac{2}{3}} + \text{H.c.}, \tag{2.3}$$

$$\mathcal{L}_{\rm Int}^{R_2^{\frac{2}{3}}} = y_{R_{\rm RL}} * \overline{t_R} v_\tau R_2^{\frac{2}{3}} + y_{R_{LR}} * \overline{b_L} \tau_R R_2^{\frac{2}{3}} + \text{H.c.}, \tag{2.4}$$

where "RL" in $y_{R_{\rm RL}}$ signifies that the chiralities of the quark and lepton are right handed and left handed, respectively. Other subscripts also carry the same convention. As $S_3^{\frac{2}{3}}$ has only one decay channel (i.e., $S_3^{\frac{2}{3}} \to t_L \nu_\tau$), it has 100% branching fraction for it. Although $R_2^{\frac{2}{3}}$ has two decay channels, in our present analysis we shall assume 100% branching fraction to its $t_R \tilde{\nu}_\tau$ decay mode, which can easily be scaled to other values as required.[7]

III. PAIR PRODUCTION AT NLO + PS ACCURACY

We consider signal events at the NLO in QCD matched to parton shower. The production of events at the NLO(FO) QCD accuracy requires calculating amplitudes of LO, virtual and real-emission Feynman diagrams. We show all the LO and a few virtual Feynman diagrams for the pair production of scalar leptoquarks in Fig. 1. The real-emission diagrams are not shown, which are tree-level diagrams with an extra gluon or light quark. The diagrams are drawn using the JaxoDraw package [54]. The events are produced using MadGraph5_aMC@NLO [55]. For the signal, we first write the model in FeynRules [56] and use the NLOCT [57] package[8] to produce the universal FeynRules output Universal FeynRules Output (UFO) model [59]. This UFO model is then used in MadGraph5_aMC@NLO to generate events at the NLO(FO) accuracy. To account for the infrared divergence in real emission processes, MadGraph5_aMC@NLO uses the FKS subtraction method [60,61].

In Table II, we show the cross sections for the production and $R_2^{\frac{2}{3}}$ are the same up to Monte Carlo uncertainty, as expected from the discussion in the previous section. Corrections due to the NLO QCD effects are around 10%. We have used `NNPDF23_lo_as_0119_qed` and `NNPDF23_nlo_as_0119_qed` parton distribution functions, respectively, for the LO and NLO calculations. The partonic center of mass energy is used as the central choice for the renormalization and factorization scales. For the scale-variation study, we vary the renormalization and factorization scales up and down by a factor of 2, resulting in total nine points including the central choice. The upper and lower envelopes of the variations of the cross section due to these different choices of scales are shown as the percentage change from the central cross section in the superscript and subscript, respectively. From the table, we see the NLO QCD correction here reduces the scale uncertainty by around a factor of 2.

The NLO(FO) results discussed in the above two paragraphs can give distributions of different kinematic variables using weighted events, but unweighting of the these events cannot be done as the matrix elements are not bounded in this case [55]. Also in this case, the result is not physical for low-p_T region. However, it can produce unweighted events while matched to the parton shower making use of the MC@NLO formalism [62]. Results at the NLO + PS accuracy give correct description of the low-p_T region. For showering of events, we use PYTHIA8 [63]. In Fig. 2, we see that NLO + PS calculation over the fixed-order one reduces

[6]The diquark coupling can also be forbidden by demanding either baryon number or lepton number conservation.

[7]For other branching fractions, the production cross section of leptoquark pair will also depend on $y_{R_{LR}}$ in the five-flavor scheme, since a t-channel production diagram will appear when $y_{R_{LR}}$ is nonzero. However, in Ref. [52] it has been shown that the dependence of the cross section on this parameter is quite small.

[8]The NLOCT package calculates the UV and R2 terms of the OPP method [58].

TABLE II. Cross sections for the pair production of scalar leptoquarks of mass $M_{LQ} = 1300$ GeV at the 14-TeV LHC. The scale variations are shown in subscript and superscript.

Order	LO (fb)	NLO(FO) (fb)
Model		
$S_3^{\frac{2}{3}}$	$0.6621^{+37.8\%}_{-25.8\%}$	$0.7229^{+14.5\%}_{-14.7\%}$
$R_2^{\frac{5}{3}}$	$0.6631^{+37.8\%}_{-25.8\%}$	$0.7163^{+14.9\%}_{-14.8\%}$

the cross section at the lower transverse momentum region of the leptoquark pair system $p_T(S_3^{+\frac{2}{3}}S_3^{-\frac{2}{3}})$ due to the Sudakov suppression.

In Fig. 3, we show LO + PS and NLO + PS normalized distributions of missing transverse energy (MET) and $\log_{10}[p_T(S_3^{+\frac{2}{3}}S_3^{-\frac{2}{3}})]$ in the upper panels of two subfigures. The shapes of MET distributions for LO + PS and NLO + PS are identical and they peak around 700 GeV. For $p_T(S_3^{+\frac{2}{3}}S_3^{-\frac{2}{3}})$ distribution in the right figure, the peak for NLO + PS is slightly shifted towards left of the LO + PS one and they peak in the range of 100–300 GeV. In the lower panels, we show the k factor for differential distribution, i.e., the ratio of differential NLO + PS cross section to the LO + PS one. In the left figure for MET, we see that for the shown range the k factor at different bins stays nearly the same and takes a value around 1.1. In the right figure, the differential k factor is not flat for $\log_{10}[p_T(S_3^{+\frac{2}{3}}S_3^{-\frac{2}{3}})]$ and therefore scaling the leading-order events by a constant k factor would not give precise results.

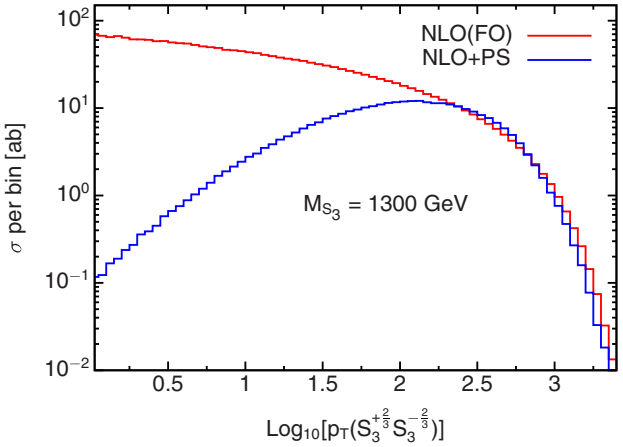

FIG. 2. Distributions of $\log_{10}[p_T(S_3^{+\frac{2}{3}}S_3^{-\frac{2}{3}})]$ for NLO(FO) and NLO matched to parton shower.

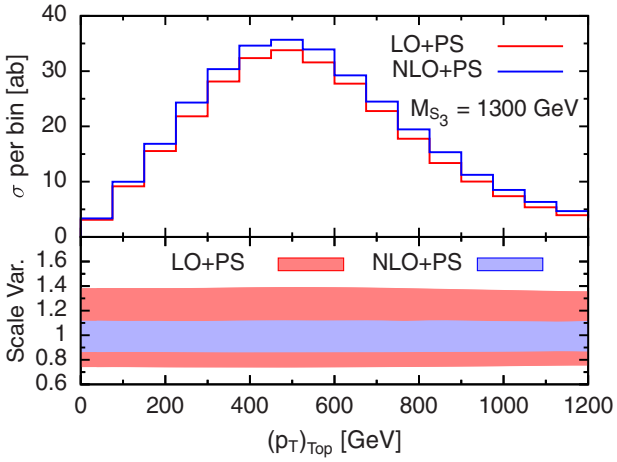

FIG. 4. In the upper panel, we show distribution of $(p_T)_{Top}$ at LO + PS and NLO + PS accuracies. The bands in the lower panel show the scale variation of the distribution with respect to central value. The bands are drawn between the envelopes of the different distributions arising from the different scale choices.

In the upper panel of Fig. 4, we show differential distribution of cross section with respect to the top transverse momentum at the LO + PS and NLO + PS level for the central scale choice. We see that the NLO + PS corrections lead to increased cross section at every bin. In the lower panel, the effect of scale variation is shown as red and blue bands, where a band is drawn between the upper and lower envelopes of different results for different

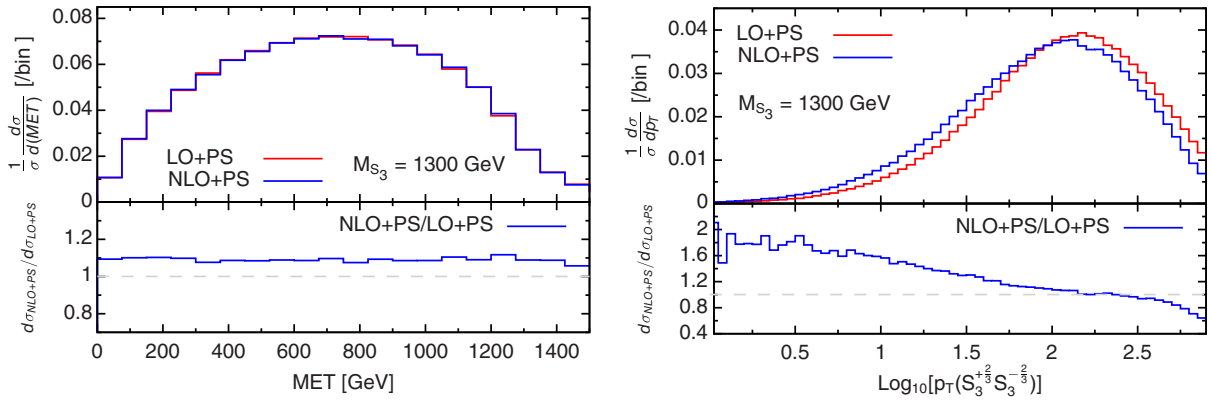

FIG. 3. The distributions of MET and $\log_{10}[p_T(S_3^{+\frac{2}{3}}S_3^{-\frac{2}{3}})]$ at LO + PS and NLO + PS.

scale choices. It can be seen that the scale variation of NLO + PS result is significantly smaller compared to the LO + PS one, confirming that the NLO QCD correction leads to a more accurate result in addition to the enhancement in the cross section.

IV. COLLIDER ANALYSIS

We consider pair production of $\frac{2}{3}e$-charged third-generation scalar leptoquarks ($S_3^{2/3}$ and $R_2^{2/3}$) and try to probe them at the 14-TeV LHC with two toplike fatjets plus large missing transverse momentum. Third-generation scalar leptoquark pair production is possible only through gluon fusion and $q\bar{q}$ annihilation, and hence the cross section is independent of any model-dependent coupling and depends only on the leptoquark mass. We consider NLO QCD corrections matched to parton shower of the LQ pair-production channel and a few representative diagrams are already shown in Fig. 1. Equations (2.3) and (2.4) show the decay modes of $S_3^{2/3}$ and $R_2^{2/3}$, respectively. We consider decay of $R_2^{2/3}$ fully into a top quark and a neutrino. Since the current ATLAS study [30] excludes the third-generation LQ of mass lower than 1.24 TeV, the top quark originating from the decay of heavy LQ will have a high boost. The top quark will decay further, and all the decay components will start collimating, resulting in a boosted large-radius jet, called top fatjet (J_t). We consider the hadronic decay of the top quarks. So, in the final state, we have two boosted toplike fatjets and a significant missing transverse momentum. We use jet substructure variables, missing energy, and other high-level observables to distinguish the signal from the SM background.[9] The signal topology is given below:

$$\begin{aligned} pp &\to S_3^{2/3} S_3^{-2/3}[\mathrm{QCD}] \to (t\nu_\tau)(\bar{t}\bar{\nu}_\tau) j \Rightarrow 2J_t + \not{E}_T + X, \\ pp &\to R_2^{2/3} R_2^{-2/3}[\mathrm{QCD}] \to (t\bar{\nu}_\tau)(\bar{t}\nu_\tau) j \Rightarrow 2J_t + \not{E}_T + X, \end{aligned} \tag{4.1}$$

where the top quarks coming from the $S_3^{2/3}$ and $R_2^{2/3}$ decay are, respectively, left and right chiral.

A. Background simulation

All the background processes that can potentially mimic the signal are included in our analysis. Each background process is generated with two to four additional QCD jets and matched according to the MLM scheme [66,67] with virtually ordered PYTHIA shower. Parton distribution function sets, renormalization, and factorization scales that are used in our analysis remain the same as described in Sec. III.

[9]Fatjets plus the missing energy signature are also searched to probe other different BSM models in the context of the LHC [64,65].

The showered events are then passed through DELPHES3 [68] for detector simulation purpose, and we use the default CMS card provided there. Particle-flow towers and tracks are clustered to form anti-kT jets of radius parameter 0.5. Fatjets (J or J_t) of radius 1.5 are constructed with the Cambridge-Achen (CA) algorithm [69] using FastJet 3.2.2 [70].

1. $t\bar{t}$ + jets

One of the main backgrounds for our signal process is the pair production of top quarks when one of the top quarks decays hadronically and the other decays leptonically. The top quark that decays hadronically is reconstructed as top fatjet. The neutrino from the leptonic decay of the other top quark and the lepton that escapes detection provide MET ($\not{E}_T$), while another fatjet comes from the QCD radiation or b jet. Hadronic decay of both top quarks can give two boosted top fatjets; however, the requirement of significant missing energy reduces this background compared to the previous setup by a factor of 100, since the MET comes from the mismeasurement of the hadronic activities. This background is produced with two additional radiations and matched with the MLM matching scheme.

2. Z + jets

Another main background of our signal is the inclusive Z-boson production, where the Z-boson decays invisibly. This process is generated with four extra partons, and the MLM matching is used. Two fatjets essentially originate from the QCD jets.

3. W + jets

It contributes considerably but is smaller than Z + jets background. When the W boson decays leptonically, the missing energy comes from the neutrino and the lepton that escape detection. This background is also generated with four partons following MLM matching and here also the fatjets come from the extra radiations.

Since our analysis requires large missing energy, we generate Z + jets and W + jets backgrounds with a generation-level hard-cut $\not{E}_T > 100$ GeV for better statistics.

4. tW + jets

Single top-quark production at the LHC in association with the W boson contributes considerably as a background, which is generated with two extra partons using MLM matching. Top quark decays hadronically to give rise to a boosted toplike fatjet, while another fatjet comes from the QCD radiation. The neutrino with the missing lepton from W decay is the source of the missing energy.

5. VV + jets

A small contribution can come from the diboson production, which can be classified into three different categories, WZ, WW, and ZZ, where all of these are

TABLE III. Higher-order QCD-corrected production cross sections of different background processes at the 14-TeV LHC used in our analysis, where the order of QCD correction is presented in brackets.

Background	References	σ (pb)
$t\bar{t}+$ jets	[71]	988.57 [N^3LO]
$tW+$ jets	[72]	83.1 [N^2LO]
$Z+$ jets	[73,74]	6.33×10^4 [N^2LO]
$W+$ jets		1.95×10^5 [NLO]
$ZZ+$ jets	[75]	17.72 [NLO]
$WW+$ jets		124.31 [NLO]
$WZ+$ jets		51.82 [NLO]

matched with two extra partons applying MLM matching scheme. WZ contributes the most among these three, where the Z boson decays invisibly to produce missing energy and hadronic decay of the W boson gives one fatjet. Even though WW and ZZ contribute almost negligibly we keep these backgrounds in our analysis. In either case, one of them decays hadronically and the other one decays leptonically (W) or invisibly (Z). In all processes, another fatjet comes due to the QCD radiation.

6. $t\bar{t}Z$

The cross section of $t\bar{t}Z$ is smaller than any of the above-mentioned background processes, but we keep this too in our analysis. This process becomes signal-like when Z boson decays invisibly and two tops are reconstructed as toplike fatjets. This process gives almost negligible contribution compared to $Z+$ jets and $t\bar{t}+$ jets backgrounds. We omit $t\bar{t}W$ background since its contribution is found to be even more suppressed.

7. QCD background

The dijet production cross section is vast at the LHC; even after constructing two fatjets, huge events remain from this background. The requirement of large missing energy gives additional suppression of order 100 since MET here can only occur due to the mismeasurement of hadronic activities. An additional suppression of order 50 comes from the requirement of b-tagged fatjet. So, QCD backgrounds are found to be negligible compared to the other backgrounds and therefore we do not include them in our analysis.

The background processes considered in our analysis are normalized with the available higher-order QCD-corrected production cross section, as presented in Table III.

B. Construction of jet substructure variables

Jet substructure variables provide good efficiencies when analyzing boosted topologies. The substructure variables that we use in our analysis are listed below.

1. Pruned jet mass

Jet mass is a good variable in separating a boosted toplike fatjet from the boosted W/Z boson or the QCD fatjets. Additional soft and wide-angle radiations from the underlying QCD interactions can contribute to the fatjet mass. So, for realistic predictions, one needs to remove those contributions. Pruning, filtering, and trimming [76–79] are different jet-grooming techniques and we use pruning in our analysis. The fatjet mass is defined as $M_J=(\sum_{i\epsilon J}p_i)^2$, where the four-momentum of the ith constituent is denoted as p_i. After clustering a fatjet using the CA algorithm, we decluster its constituents in each recombination step and remove the soft and wide-angle radiations from the fatjet. The merging of ith and jth protojets into the fatjet is vetoed, and the softer one is removed, if the following conditions are achieved:

$$Z=\min(P_{Ti},P_{Tj})/(P_{Ti}+P_{Tj})<Z_{\rm cut},\quad \text{and}\quad \Delta R_{ij}>R_{\rm fact}. \tag{4.2}$$

The angular separation between two protojets is ΔR_{ij}, and we choose $R_{\rm fact}=0.86\sim\frac{m_{\rm top}}{P_{T,\rm top}}$ [79]. Z and P_{Ti} are the softness parameter and the transverse momentum of the ith protojet, respectively. We set $Z_{\rm cut}=0.1$ [78] in our analysis.

2. N-subjettiness ratio

N-subjettiness is a jet shape variable that measures how the energy of a fatjet is distributed around different subjet axes and is defined as follows [80,81]:

$$\tau_N=\frac{1}{\mathcal{N}_0}\sum_i P_{T,i}\min\{\Delta R_{i,1},\Delta R_{i,2},\cdots\Delta R_{i,N}\}. \tag{4.3}$$

The summation runs over all the constituent particles of the jet. $\mathcal{N}_0$ is the normalization factor, defined as $\mathcal{N}_0=\sum_i P_{T,i}R$, where $P_{T,i}$ is the transverse momentum of the ith constituent of the jet of radius R. $\Delta R_{i,K}=\sqrt{(\Delta\eta)^2+(\Delta\phi)^2}$ is the angular separation of the ith constituent of the jet from its Kth-subjet axis in the pseudorapidity-azimuthal angle, i.e., $\eta-\phi$ plane. Rather than τ_N, the ratio $\frac{\tau_N}{\tau_{N-1}}$ is a more effective discriminating variable between N-prong fatjets and SM background [80]. Our analysis uses $\tau_{32}=\frac{\tau_3}{\tau_2}$ and $\tau_{31}=\frac{\tau_3}{\tau_1}$ to differentiate top fatjets from the SM background.

C. Event selection

1. Baseline-selection criteria

We apply the following preselection cuts (C1) to select events for further analysis.

(i) The radius parameter of the top fatjet is $R\sim\frac{2m_t}{P_T}$, where P_T and m_t are the transverse momenta and top

TABLE IV. The expected number of events (in fb, multiplying with the luminosity gives the expected event numbers) and cut efficiency for the signal S_3 and R_2 (1.3-TeV mass of leptoquark for both models) and all the background processes that contribute to the fatjets $+\not{E}_T$ final state after implementing the corresponding cuts at the 14-TeV LHC are shown. The effectiveness of different kinematic cuts can be followed from top to bottom after applying (C1) preselection cuts, (C2) $\not{E}_T > 150$ GeV, (C3) requiring at least one b tag within J_0 or J_1, and finally (C4) $M_{J_0}, M_{J_1} > 120$ GeV. After applying C4 cut, the remaining events are passed for the multivariate analysis.

Cuts	S_3 (fb)	R_2 (fb)	$Z+$jets (fb)	$W+$jets (fb)	$t\bar{t}+$jets (fb)	$tW+$jets (fb)	$WZ+$jets (fb)	$WW+$jets (fb)	$ZZ+$jets (fb)	$t\bar{t}Z$ (fb)	Total BG (fb)
C1	0.2315 [100%]	0.232 [100%]	2517.99 [100%]	1366.91 [100%]	690.65 [100%]	366.91 [100%]	93.53 [100%]	25.90 [100%]	11.51 [100%]	5.24 [100%]	5078.64 [100%]
C2	0.2258 [97.54%]	0.2262 [97.5%]	1640.29 [65.14%]	762.59 [55.79%]	302.16 [43.75%]	152.52 [41.57%]	58.35 [62.39%]	11.51 [44.44%]	6.973 [60.58%]	3.96 [75.57%]	2938.36 [57.86%]
C3	0.1810 [78.19%]	0.1801 [77.63%]	241.73 [9.60%]	117.99 [8.63%]	230.94 [33.44%]	114.39 [31.18%]	10.79 [11.54%]	2.45 [9.46%]	1.92 [16.69%]	3.28 [62.60%]	723.48 [14.25%]
C4	0.1047 [45.23%]	0.1033 [44.53%]	25.38 [1.01%]	17.33 [1.27%]	64.23 [9.30%]	27.45 [7.48%]	1.24 [1.33%]	0.33 [1.27%]	0.2 [1.74%]	1.474 [28.13%]	137.634 [2.71%]

quark's mass, respectively. For each event, we reconstruct at least two fatjets using CA algorithm of radius parameter 1.5 with minimum transverse momentum $P_T(J_0), P_T(J_1) > 200$ GeV.

(ii) The missing energy of each event should be greater than 100 GeV.

(iii) Since lepton is not present in the final state of our signal, we veto the events which contain any lepton of transverse momentum $P_T(l) > 10$ GeV and pseudorapidity $|\eta(l)| < 2.4$.

(iv) A minimal cut on the azimuthal separation between any fatjet and the missing momentum $\Delta\phi(J_i, \not{E}_T) > 0.2$ is applied to minimize the hadronic mismeasurement contribution.

2. Final selection cuts

After the primary selection, we apply the following cuts before passing events for multivariate analysis (MVA):

(C2) Missing energy cut is raised from 100 to 150 GeV, which reduces the background sharply.

(C3) We tag the leading b jet inside J_0 or J_1.

(C4) We demand pruned mass of both the leading M_{J_0} and subleading M_{J_1} fatjets to be greater than 120 GeV.

Table IV displays the cut flow along with the cut efficiencies, anticipated number of events (in fb, multiplying with the luminosity gives the expected event numbers) for the signal and the background processes for the 14-TeV LHC. One can see that the higher missing energy cut, b tagging within a fatjet, and the pruned fatjet masses are very effective in significantly reducing backgrounds while maintaining good signal acceptance. The principal backgrounds $Z+$ jets and $W+$ jets are drastically reduced when a b jet is tagged within the leading or subleading fatjet, and their effects are nearly identical to that of the $t\bar{t}+$ *jets* background (see the rows up to C3 in Table IV).

The normalized distributions of various kinematic variables of the signal S_3 and R_2, as well as binwise stacked histograms of all background processes after imposing $\not{E}_T > 150$ GeV and b tagging inside J_0 or J_1, together with preselection cuts, are shown in Fig. 5, where leptoquark mass is set at 1.3 TeV. The contributions of individual background processes are represented by different colors: blue, green, orange, olive, and magenta, for $t\bar{t}+$ jets, $Z+$ jets, $W+$ jets, $tW+$ jets, and $t\bar{t}Z$, respectively. Each background process is weighted by its effective cross section after applying the cuts listed and normalized to the total cross section.

The distributions of the leading and subleading fatjets' pruned masses are depicted in Figs. 5(a) and 5(b), respectively. $Z+$ jets background demonstrates no peak in the M_{J_0} and M_{J_1} distributions, near the Z-boson mass, or around the top mass as expected, since the fatjets originate from the QCD radiations. One of the tops in the $t\bar{t}+$ jets background decays hadronically and is reconstructed as a top fatjet, while the other fatjet comes because of the QCD radiation. As a result, the M_{J_0} distribution exhibits a peak near the top mass, but the M_{J_1} distribution does not exhibit a peak near the top mass.

It is also interesting to note that fatjet-mass distributions are slightly different for the two signals while other kinematic variables remain similar. This is a direct implication of two different polarizations. The bottom quark and the W boson travel in the opposite direction in the top quark's rest frame to conserve the linear momentum. As in the S_3 model the top quark is left chiral; the majority of the b quark in the top quark's rest frame lies in the same direction of the boost (this will be further discussed in the next section). This means that the majority of the W boson emerges at an angle greater than 90° to the boost. However, in the R_2 model (top quark is right chiral), most of the b quarks are found in the direction opposite to the boost in the

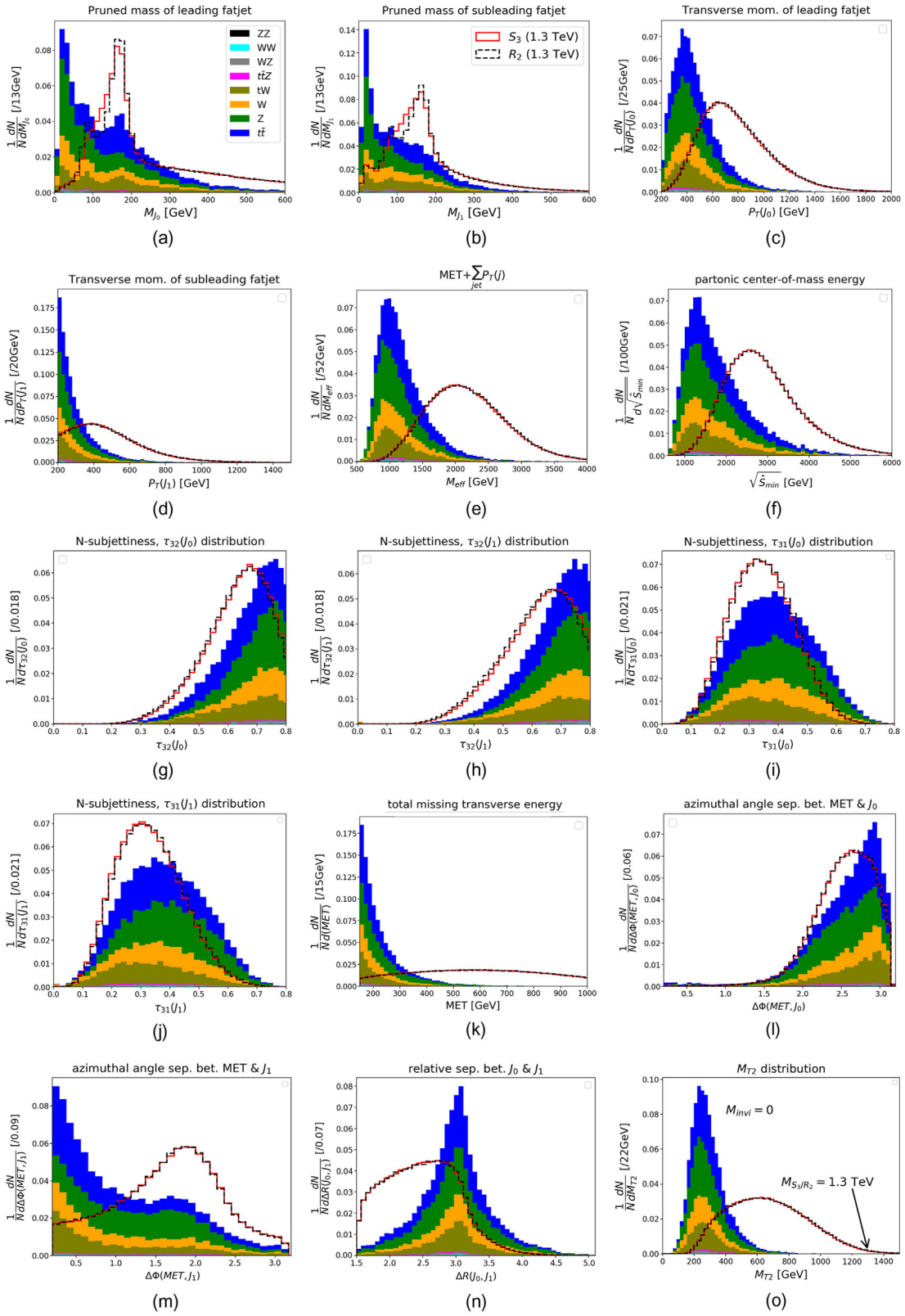

FIG. 5. After imposing $\not{E}_T > 150$ GeV and b tagging inside J_0 or J_1, together with preselection cuts as indicated in the text, the normalized distribution of kinematic variables of the signal S_3 (solid red), R_2 (dashed black), and binwise stacked histogram of all the background processes are shown.

top quark's rest frame. This suggests that most of the W bosons exist around the boost direction. As a result, in the lab frame, the quarks from the hadronic decay of the W boson are more collimated in the R_2 model compared to the S_3 model. When W and the b quark get combined to form a single large-radius three-prong fatjet, the S_3 model produces fewer events than the R_2. Because the W boson is heavier than the b quark, S_3 needs more boost to bring back all the W bosons along the boost direction compared to R_2. As a result, the R_2 model exhibits larger peaks in both the leading and subleading fatjet-mass distributions around the top-quark mass than the S_3 model. Moreover, for the R_2 model, we observe also a distinct peak at the W-boson mass in either of the fatjet mass distributions. This is because most R_2 events carry W bosons along the boost direction in the top quark's rest frame, and in lab frame decay products of W boson are more collimated compared to S_3 events. However, we see more S_3 events than R_2 between the W boson and top-quark mass because the overall cross section is the same for both models.

Figures 5(c) and 5(d), respectively, depict the transverse momentum of J_0 and J_1. From these distributions, we can observe that the signal is substantially harder than the background. Figure 5(e) displays the M_{eff} distribution, where M_{eff} is the scalar sum of the total transverse momentum of the visible jets plus MET:

$$M_{\text{eff}} = \not{E}_T + \sum |\vec{P}_{iT}|, \tag{4.4}$$

where the summation runs over all the visible jets and $\vec{P}_{iT}$ is the transverse momentum of the ith jet. Global and inclusive quantities are used to define $\sqrt{\hat{s}_{\text{min}}}$ [82], the minimum partonic center-of-mass energy, and its distribution is shown in Fig. 5(f). Neutrinos are the missing particles in our system, and the definition of $\sqrt{\hat{s}_{\text{min}}}$ is given by

$$\sqrt{\hat{s}_{\text{min}}} = \sqrt{E^2 - P_Z^2} + \not{E}_T, \tag{4.5}$$

where E and P_Z are the total energy and longitudinal component of the total visible momentum in the event, respectively. Here, visible means all the visible objects in the detector, e.g., jets, electrons, photons, and muons. The signal has a peak towards a larger value of $\sqrt{\hat{s}_{\text{min}}}$ compared to the background since the signal requires more partonic center-of-mass energy to produce two heavy LQs that subsequently decay into the top quark and neutrino.

The N-subjettiness variables, τ_{32}, for both the leading and subleading fatjets are shown in Figs. 5(g) and 5(h). τ_N tries to quantify the number of subjets inside the fatjet. One would anticipate a smaller value of τ_{32} for a boosted top fatjet since the value of τ_3 for a three-prong fatjet is small and the value of τ_2 is large; therefore, their ratio produces a smaller value. In contrast, backgrounds are mostly QCD dominated (one prong) or coming from the weak bosons (two prong), so the value of τ_2 is small for both QCD jets and fatjets originating from weak bosons, giving larger τ_{32}. The distributions show that the signal has considerably lower τ_{32} values[10] than the backgrounds, indicating that the signal has a more three-prong structure than the background. Different chirality of the top quarks accounts for the slight difference in these distributions for S_3 and R_2 models. The distributions of τ_{31} for J_0 and J_1 are shown in Figs. 5(i) and 5(j). The distributions show that both the signal and the background peak at a lower value of τ_{31}, indicating that it is not as good as τ_{32} for distinguishing the signal from the background.

The distribution of missing transverse momentum is shown in Fig. 5(k), where the background can be seen to drop sharply for large MET. In the case of signal, both the neutrinos from the decay of LQs have equal access to the phase space, resulting in a nearly uniform distribution of the missing transverse momentum. Figures 5(l)–5(n) show, respectively, the distributions of the azimuthal separation of the leading and subleading fatjets from the $\not{E}_T$ and the relative separation between the fatjets in the η-ϕ plane. The distribution of M_{T2} [83,84] is shown in Fig. 5(o). M_{T2} is useful in measuring the mass of the parent particle, which is pair produced at the collider, and subsequently decays into one visible object and one missing particle from the end point of the distribution, and it is defined as follows:

$$M_{T2} = \min_{\overrightarrow{p_{1T}}^{\text{invi}} + \overrightarrow{p_{2T}}^{\text{invi}} = \not{E}_T} [\max\{M_T^{(1)}, M_T^{(2)}\}]. \tag{4.6}$$

$M_T^{(i)}$ $(i = 1, 2)$ are the transverse masses of the LQ and anti-LQ as defined below:

$$(M_T^{(i)})^2 = m_i^2 + M_{\text{invi}}^2 + 2(E_{iT}E_{iT}^{\text{invi}} - \overrightarrow{p_{iT}} \cdot \overrightarrow{p_{iT}}^{\text{invi}}), \quad \{i = 1, 2\}. \tag{4.7}$$

Since LQ decays into a top quark and massless neutrino, we set $M_{\text{invi}}^2 = M_\nu^2 = 0$ and $E_{iT}^{\text{invi}} = |\overrightarrow{p_{iT}}^{\text{invi}}|$, where $\overrightarrow{p_{iT}}^{\text{invi}}$ is the transverse momentum of an individual neutrino. $\overrightarrow{p_{iT}}^{\text{invi}}$ is constrained by the measured missing transverse momentum,

$$\overrightarrow{p_{1T}}^{\text{invi}} + \overrightarrow{p_{2T}}^{\text{invi}} = \overrightarrow{\not{E}_T}. \tag{4.8}$$

m_i and $\overrightarrow{P_{iT}}$ $(i = 1, 2)$ are the reconstructed mass and the transverse momentum of the (sub)leading top fatjets, respectively. E_{iT} is the transverse energy of the fatjets defined as $E_{iT} = \sqrt{m_i^2 + \overrightarrow{P_{iT}}^2}$. One can observe from the

[10]Although the signal peaks at a lower value of τ_{32} than the background, the peak emerges at roughly 0.6, which is rather substantial. The three subjets of the top quark are highly collimated; therefore, the τ_2 value is also small for the top fatjets, which causes the three-prong top-fatjet's peak to arise for the signal at a significantly large value of τ_{32}.

distribution in Fig. 5(o) that its end point correctly predicts the mass of the LQ (1.3 TeV). Since the SM particles have masses that are significantly less than the LQ mass, the background and signal distributions are quite well separated. So, this variable not only predicts LQ mass, but also helps in background reduction.

D. Multivariate analysis

In the previous subsection, distribution of several observables (without C4 cut), which can be used as input variables for sophisticated multivariate analysis using the gradient-boosting technique, are described. For MVA input, we use a loose cut (up to C4), as mentioned in the preceding subsection. The last row of Table IV shows the estimated amount of signals (in fb) from two models, the contribution of different background processes, and the total background at the 14-TeV LHC after applying MVA selection cut (C4). For MVA, we use the adaptive boosted decision tree (BDT) algorithm and construct two statistically independent signal and background event samples. The background is the weighted sum of individual SM background processes. MVA picks a subset of kinematic variables from a larger collection based on the linear correlation among the variables and their relative importance in distinguishing the signal from the background.

As expected by Eq. (4.4), we notice that $P_T(J_0)$ and $P_T(J_1)$ have large correlations with $M_{\rm eff}$, and $\sqrt{\hat{s}_{\rm min}}$ also exhibits high correlations with $M_{\rm eff}$ due to their linear dependence on MET, as shown by Eqs. (4.4) and (4.5). We keep $M_{\rm eff}$ because of its high relative importance compared to $P_T(J_0)$, $P_T(J_1)$, and $\sqrt{\hat{s}_{\rm min}}$. A high correlation exists between M_{T2} and MET; however, we retain MET because it has the highest relative importance than any other variables in separating the signal from the background. Although $M_{\rm eff}$ and MET exhibit a significant correlation in both the signal and background [as predicted by Eq. (4.4)], we keep them both in our study since they have exceptionally high separation powers to distinguish the signal from the

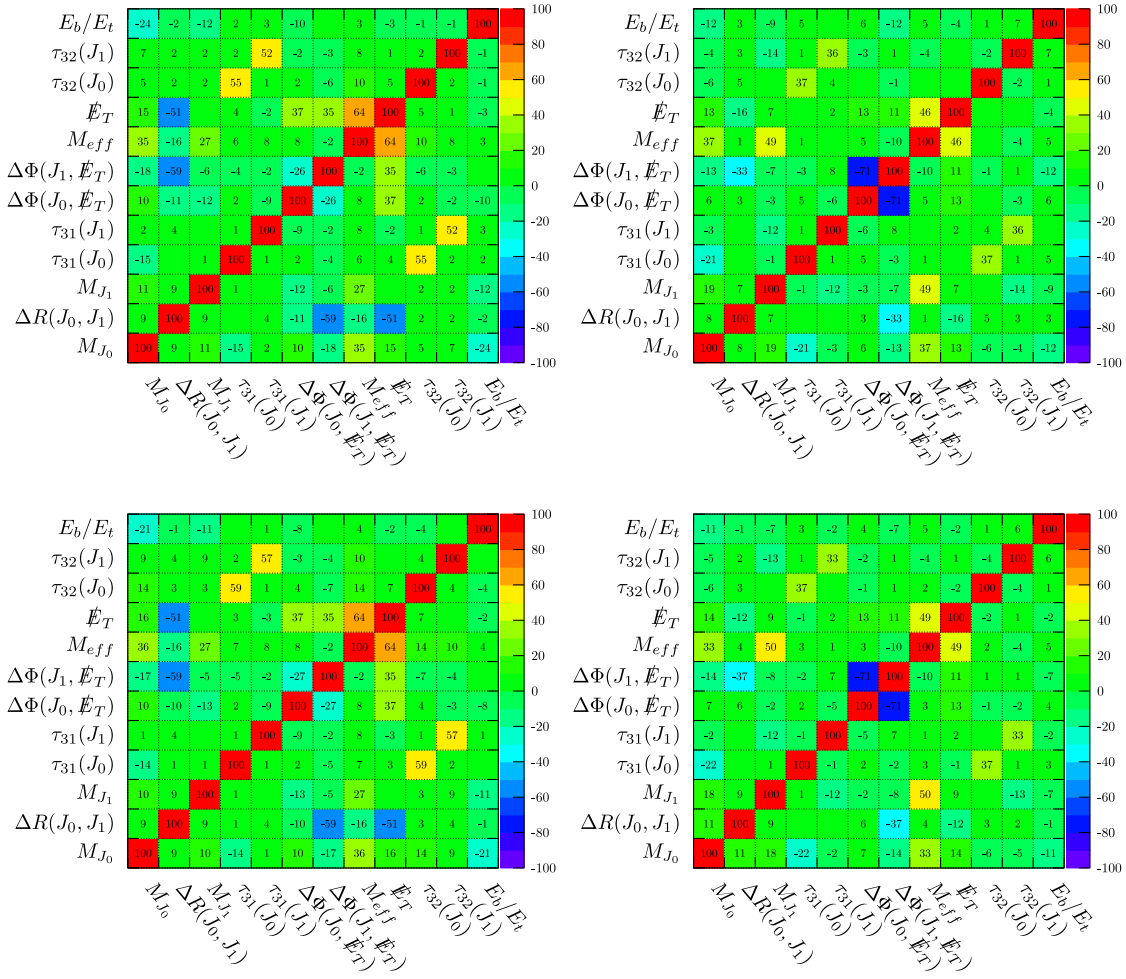

FIG. 6. Linear correlation coefficients (%) between different variables for signal S_3 (top left panel) and corresponding background (top right panel); same for signal R_2 (bottom left panel) and corresponding background (bottom right panel). Positive and negative coefficients show that two variables are correlated or anticorrelated, respectively. Missing entries indicate an insignificant correlation of less than 1.

TABLE V. Before employing at MVA, the method of unspecific relative importance (separation power) of the individual variables.

Variable	$\not{E}_T$	M_{eff}	$\Delta R(J_0, J_1)$	$\Delta\phi(J_1, \not{E}_T)$	$M(J_0)$	$\tau_{32}(J_1)$	$\tau_{32}(J_0)$	$\Delta\phi(J_0, \not{E}_T)$	$M(J_1)$	$\tau_{31}(J_1)$	$\tau_{31}(J_0)$
S_3	59.98	49.43	23.44	21.42	5.99	4.15	3.99	3.83	2.33	0.99	0.95
R_2	59.33	50.63	21.97	20.87	6.42	5.85	4.82	4.36	2.49	1.49	1.11

background. Figure 6 exhibits the linear correlation coefficients between different variables for signal S_3 (top left panel) and the corresponding background (top right panel). The bottom left and bottom right panels depict the signal R_2 and its corresponding background. Positive and negative coefficients indicate whether two variables are correlated or anticorrelated. In the TMVA package [85], the linear correlation coefficient is calculated using the following formula:

$$\rho(x, y) = \frac{\text{cov}(x, y)}{\sigma_x \sigma_y}, \tag{4.9}$$

where the covariance between x and y is $\text{cov}(x, y) = \langle xy \rangle - \langle x \rangle \langle y \rangle$ and σ_x, σ_y are the standard deviation of these variables.

The separation power of different kinematic variables for the two models used in MVA is presented in Table V. This table shows that the order of the variables for distinguishing the leptoquark signal from the overwhelming background are the MET, M_{eff}, relative separation between the fatjets in η-ϕ plane, and azimuthal separation between the subleading fatjet and MET. Due to improper selection of various (BDT-specific) parameters during training, the BDT method may result in overtraining. Overtraining can be prevented if the Kolmogorov-Smirnov probability is checked throughout training. We train the algorithm separately for the S_3 and R_2 models and ensure that there is no overtraining in our analysis. The top left panel of Fig. 7 shows the normalized distribution of the BDT output for the signal S_3 (blue) and its background (red) for both training and testing samples, whereas the

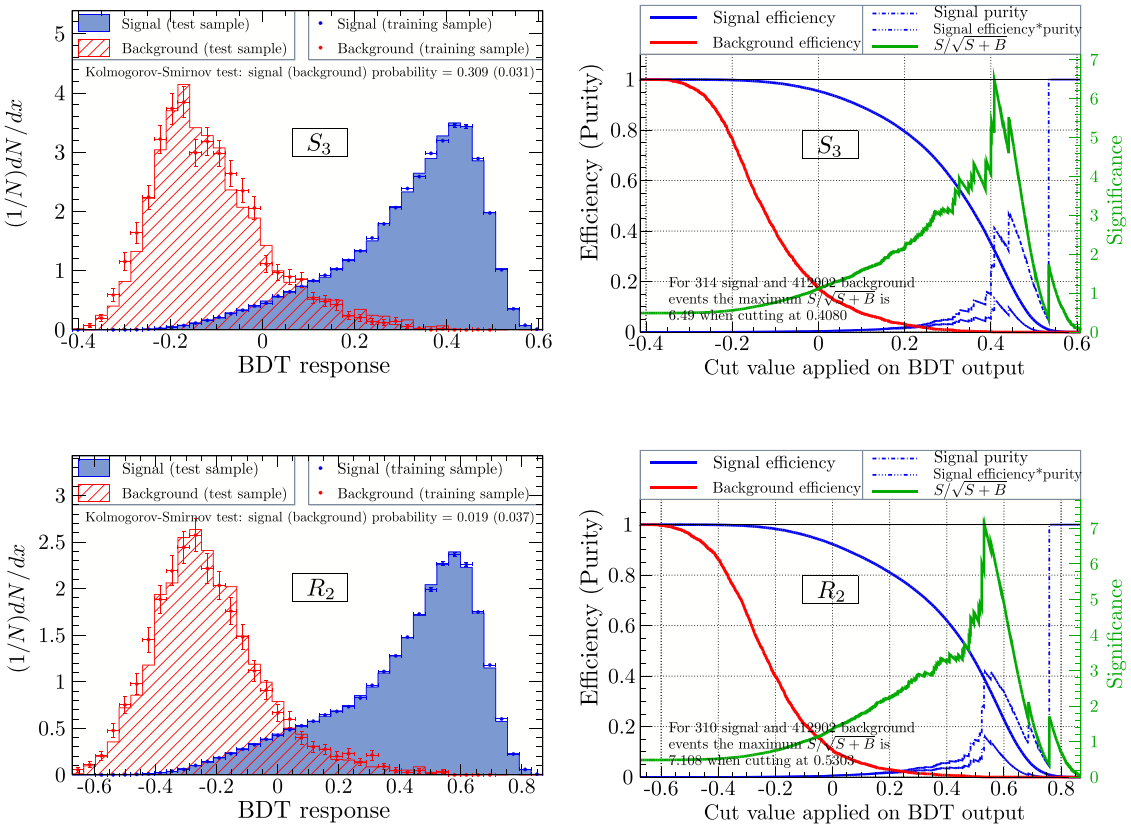

FIG. 7. The top left plot depicts the distribution (normalized) of the BDT output for the training and testing samples for both the signal S_3 (blue) and background (red) classes. The right plot depicts signal S_3 (blue) and background (red) efficiencies, as well as statistical significance ($\frac{N_S}{\sqrt{N_S+N_B}}$) as a function of the cut applied to BDT output. The same for the R_2 model is shown in the bottom left and bottom right plots.

TABLE VI. The table shows the effectiveness of the present search in terms of statistical significance for S_3 and R_2 models. Before applying any cuts to the BDT output, the total number of events for different models and the combined background are N_S^{bc} and $N_{\rm SM}$, respectively (as shown in Table IV). For the 14-TeV LHC, after employing an optimum cut (BDT$_{\rm opt}$) on the BDT response, the surviving number of signal and background events are provided by N_S and N_B (in fb), respectively. For quick access, the statistical significances corresponding to 3-ab^{-1} luminosity are also shown.

	N_S^{bc} (fb)	BDT$_{\rm opt}$	N_S (fb)	N_B (fb)	$\frac{N_S}{\sqrt{N_S+N_B}}$ ($\frac{N_S}{\sqrt{N_B}}$), 3 ab^{-1}	$\frac{N_S}{N_B}$
S_3	0.1047	0.4080	0.03403	0.04850	6.5 (8.5)	0.702
R_2	0.1033	0.5303	0.04047	0.05677	7.1 (9.3)	0.713
$N_{\rm SM}$	137.634					

TABLE VII. Discovery and exclusion reach at 14-TeV LHC for 3-ab^{-1} luminosity.

$\mathcal{L} = 3$ ab^{-1}	$S_3^{\frac{2}{3}}$	$R_2^{\frac{2}{3}}$
5σ discovery	1380 GeV	1370 GeV
2σ exclusion	1520 GeV	1520 GeV

TABLE VIII. Spin-analyzing power of bottom quark and W^+ coming from top decay.

Daughters	b	W^+
k_i	−0.41	+0.41

bottom left plot shows the same for the $R2$ model. We observe that for both models, signal and background are well separated. In the same figure, the top right plot illustrates the signal S_3 (blue) and background (red) efficiencies, as well as statistical significance (green) as a function of the cut applied to BDT output, while the bottom right plot depicts the same for the R_2 model.

The statistical significance of the two models at 3-ab^{-1} integrated luminosity at the 14-TeV LHC and the signal-to-background ratio are shown in Table VI. There, N_S^{bc}[11] and $N_{\rm SM}$ represent the total number of events for the signal and background before applying any cut to the BDT output, while N_S and N_B represent the same after applying an optimal cut BDT$_{\rm opt}$ to the BDT response. We observe that both models at the HL-LHC have discovery potential for the 1.3-TeV scalar leptoquark. The 5σ discovery and 2σ exclusion limits of these two models at the HL-LHC are presented in Table VII. There is a slight difference in the discovery potential of these two models because of their polarization. Note that explicitly the polarization variables have a negligible role compared to other variables such as MET, $\Delta R(J_0, J_1)$, etc., as given in Table V for discovering the leptoquark signal at the LHC. However, we see significant differences in the J_0 and J_1 mass distribution and slight in N-subjettiness distributions because of the different chirality of the top quarks of the two models. So, once the LQ signal is discovered at the LHC, we can use the polarization variables to distinguish these two models, which are described in detail in the next section. In our analysis, we find that a scalar LQ of mass 1270 GeV or smaller can be rejected with 2σ with an integrated luminosity of 140 fb^{-1}, which is compatible with the existing ATLAS search and analysis. We also find that a luminosity around 1600 fb^{-1} is required for the 5σ discovery of 1.3-TeV scalar LQ.

[11]Although we use full NLO events, if one uses LO events but normalizes with the total NLO cross section, N_S^{bc} number for both models decreases by around 2%.

V. DISTINGUISHING TWO MODELS

If a leptoquark signature is observed at the collider in some particular final state, the next goal will be to distinguish different models in order to probe its genesis. In the above section, we have seen that pair production in both $S_3^{\frac{2}{3}}$ and $R_2^{\frac{2}{3}}$ models can finally give two fatjets plus large missing energy signature. The leptoquarks in these two models decay to top quarks of different helicities. Top quark's polarization can be probed by studying the distribution of some particular kinematic variables of its decay products, which can in turn allow us to probe the type of the leptoquark. In the following subsection, we discuss some such polarization variables that can address the leptoquark identity.

A. Polarization variables

There are different variables which can exhibit dependence on top-quark polarization. In the following, we discuss a few of them.

1. Angular variable in the rest frame of (anti-)top

In the rest frame of top quark, if θ_i is the angle between the decay particle i and the direction of boost of the top quark, the differential distribution of the decay width Γ with respect to the angular variable $\cos\theta_i$ is given by

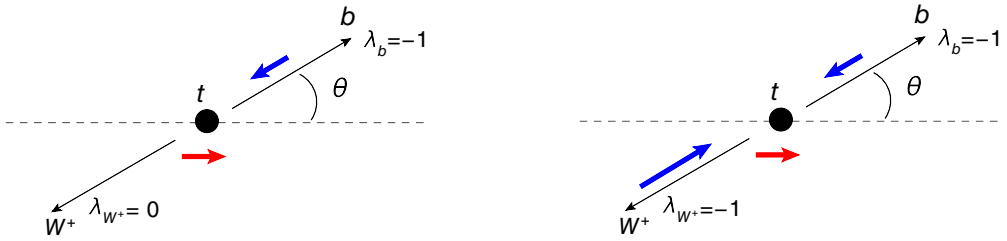

FIG. 8. Decay diagram of right-handed top quark in its rest frame. Black dot represents top quark. Thick colored arrows denote spin of the particles. For b quark, essentially $\lambda_b = -1$ component gets produced and the other component $\lambda_b = +1$ is heavily suppressed, because of its small mass. The top decays to $\lambda_{W^+} = 0$ and $\lambda_{W^+} = -1$ helicity components of W^+ 70 and 30% times, respectively. As the other transverse component W boson, i.e., $\lambda_{W^+} = 1$, requires right-handed b quark to conserve spin, it is also suppressed. So, in effect only the two diagrams shown here contribute to the right-handed top-quark decay.

$$\frac{1}{\Gamma}\frac{d\Gamma}{d\cos\theta_i} = \frac{1}{2}(1 + \mathrm{P}_t \mathrm{k}_i \cos\theta_i), \tag{5.1}$$

where P_t is the top-quark polarization, which is $+1$ for the right-handed top and -1 for the left-handed top. k_i is the spin-analyzing power of the ith decay particle. In Table VIII, we show the spin-analyzing power of different decay particles. In Appendix A 1, the spin-analyzing power of bottom quark is derived. Similar distribution in the antitop rest frame can be written as

$$\frac{1}{\bar{\Gamma}}\frac{d\bar{\Gamma}}{d\cos\bar{\theta}_{\bar{i}}} = \frac{1}{2}(1 + \bar{\mathrm{P}}_{\bar{i}} \bar{\mathrm{k}}_{\bar{i}} \cos\bar{\theta}_{\bar{i}}), \tag{5.2}$$

where the entities with bars are the corresponding quantities for the antitop quark. Here as well, $\overline{P}_{\bar{i}}$ is $+1$ for right-handed antitop and -1 for left-handed antitop. $\bar{k}_{\bar{i}}$ is given by $\bar{k}_{\bar{i}} = -k_i$. So, it is evident that the distribution of the ith decay particle coming for the right-handed top will be the same as the distribution of the $\bar{i}$th decay product of the left-handed antitop. As we are producing leptoquark pair which will decay to top and antitop with opposite helicities, this feature will ensure the distributions of b and $\bar{b}$ for a model are the same.

The decay of top quark gives rise to mostly left-handed ($\lambda_b = -1$) b quark and the other component, i.e., the right-handed one, is heavily suppressed because of small mass of b quark.[12] It is known that the top quark decays 70% of the time to longitudinal ($\lambda_{W^+} = 0$) and 30% of the time to one of the transverse ($\lambda_{W^+} = -1$) components of the W boson [86,87].[13] So for top quark, essentially only two decay configurations exist. In Fig. 8, to illustrate, we show these two configurations for decay of a right-handed top quark in its frame. To conserve the total spin in the decay process, the total spin of the b-quark and W- boson system must be equal to $\frac{1}{2}$. Moreover, we can write the spin state of the b-quark and W-boson system in the basis of $|+\rangle_{\hat{z}}$ and $|-\rangle_{\hat{z}}$ states[14] (with positive z axis along the top-boost direction). So, to conserve the third component of spin, only the $|+\rangle_{\hat{z}}$ component can contribute, as the top-quark spin is along the boost direction. For the left diagram, the total spin of b-quark and W-boson system makes an angle $(180 - \theta)$ with the boost direction, whereas for the right diagram it makes angle θ. So, the left diagram follows a $\sin^2\frac{\theta}{2}$ distribution, whereas the right diagram follows a $\cos^2\frac{\theta}{2}$ distribution.[15] Obviously, the weighted sum of these two distributions should lead to Eq. (5.1).[16]

2. Energy variables in the lab frame

In the literature [40,45,48,50], two most-discussed energy variables for the polarization study are $z = \frac{E_b}{E_t}$ and $u = \frac{E_l}{(E_l+E_b)}$. However, the variable $z = \frac{E_b}{E_t}$, which is the fraction of energy of the top quark carried by the b quark in the lab frame, is only the relevant one here as the W boson originating from the top quark decays hadronically in our study. The variable "z" and $\cos\theta_b$ are fully correlated and they are related by the following relation [40] (see Appendix A 2):

$$\cos\theta_b = \frac{1}{\beta_t}\left(\frac{2m_t^2}{m_t^2 - m_W^2} z - 1\right), \tag{5.3}$$

where β_t represents the boost of the top quark in the lab frame. The distribution of decay width with respect to z [using Eqs. (5.1) and (5.3)] can be given as [48]

[12]This happens as the decay is governed by weak interaction, which couples to only left-handed fermions in the massless limit.

[13]The top-quark decay to the other transverse component ($\lambda_{W^+} = +1$) is almost negligible, as this requires right-handed b quark (which is heavily suppressed) to conserve spin angular momentum.

[14]$|+\rangle_{\hat{n}} = \cos\frac{\Theta}{2}|+\rangle_{\hat{z}} + \sin\frac{\Theta}{2} e^{i\Phi}|-\rangle_{\hat{z}}$, where $\hat{n}$ is a unit vector along (Θ,Φ) direction.

[15]$(\cos\frac{\Theta}{2})^2|_{\Theta=180-\theta} = \sin^2\frac{\theta}{2}$.

[16]$0.7\ \sin^2\frac{\theta}{2} + 0.3\cos^2\frac{\theta}{2} = 0.5 - 0.2\cos\theta$.

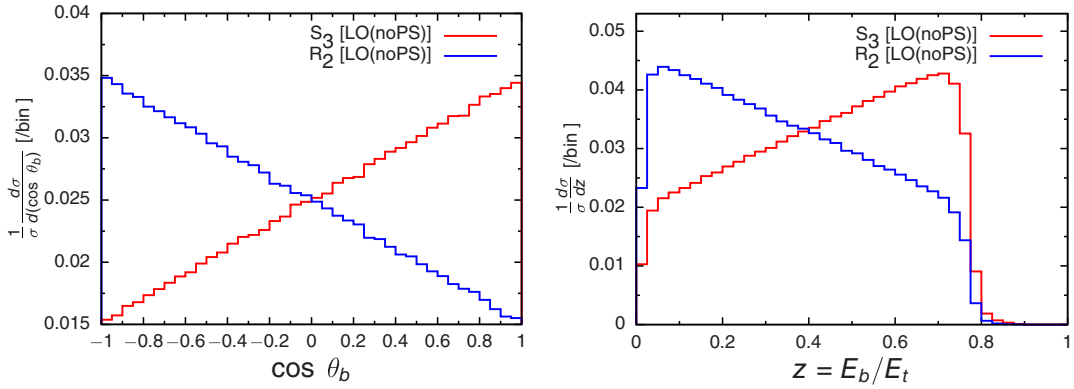

FIG. 9. The distributions of $\cos\theta_b$ and $\frac{E_b}{E_t}$ at LO without parton shower. The mass of the leptoquark has been taken to be 1300 GeV.

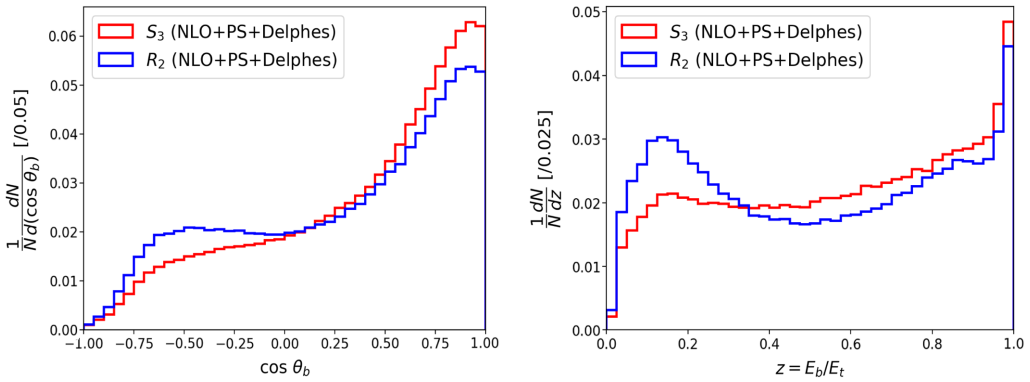

FIG. 10. The distributions of $\cos\theta_b$ and $\frac{E_b}{E_t}$ after DELPHES simulation and applying cuts up to C4 mentioned in Sec. IV C. The effect of radiation causes significant changes in the distribution compared to truth-level results. For $\cos\theta_b \sim 1$ and for z around 0.8 and more, the distributions are strikingly different from the truth-level results because of the contamination in the b jet from W- decay products, owing to very large boost of top quark.

$$\frac{1}{\Gamma}\frac{d\Gamma}{dz} = \frac{1}{\beta_t}\frac{m_t^2}{m_t^2 - m_W^2}\left(1 - P_t k_f \frac{1}{\beta_t} + P_t k_f \frac{1}{\beta_t}\frac{2m_t^2}{m_t^2 - m_W^2} z\right). \tag{5.4}$$

The similar expression will hold for antitop particle with every element replaced by their corresponding barred element.

3. Distributions of polarization variables

In Fig. 9, we show truth-level normalized distributions of $\cos\theta_b$ and $\frac{E_b}{E_t}$ at LO at the left and right subfigures, respectively.[17] The distribution with respect to $\cos\theta_b$ can be understood from Eq. (5.1). Therefore, in S_3 model, for most of the events in the rest frame of the top quark, the b quark moves in the same direction as the boost of the top quark. Obviously, the opposite happens for the R_2 model. For the $z = \frac{E_b}{E_t}$ variable, we see for the S_3 and R_2 models, the distribution peak near the right and left end of the plots, respectively. This can also be understood from the $\cos\theta_b$ distribution. As for the R_2 model, in the rest frame, for majority of events, the b quarks move in the direction opposite to the boost and their energy E_b will be less. Therefore, the distribution in this case peaks towards the left. The reverse happens for the S_3 model. Another interesting thing to observe in the right figure is that the cross section is zero after $z = 0.8$. This happens because all the top-quark energy cannot be carried by the b quark only, as the W boson needs at least its rest mass energy, M_W. In Fig. 10, we show these distributions after including NLO calculation, showering effect, and applying various cuts up to C4 (discussed in Sec. IV C) in DELPHES simulation. Here, the distribution of b jet is found to be different from that of b quark because of showering effects and formation of jets. Near the boost direction, i.e., near $\cos\theta_b \sim 1$, the difference between the b-quark and b-jet distributions is striking as there b jet gets contaminated with the particles originating from W boson because of very large boost of top quark.

[17] As discussed in Sec. V A 1, b and $\bar{b}$ jets have the same distributions for a model. For an event, now onwards by b we will mean either b or $\bar{b}$ jet and t will mean corresponding top or antitop fatjet.

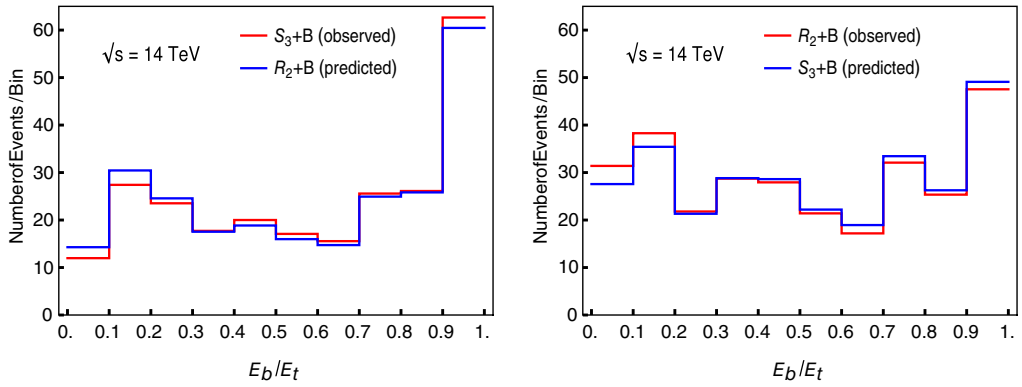

FIG. 11. The signal + background event distributions in $\frac{E_b}{E_t}$ for observed and predicted model data after applying an optimal BDT cut (given in Table VI) with 3000 fb^{-1}. To find the events for the predicted model, the signal events of it are passed through the same BDT model used for finding the event numbers of the observed model.

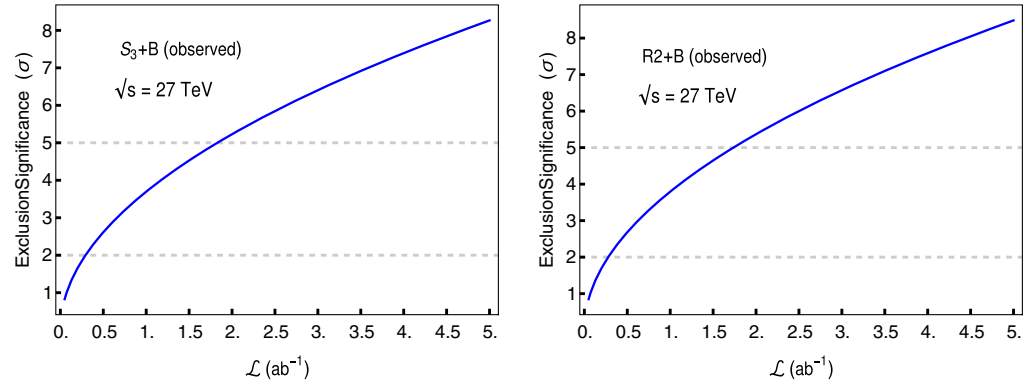

FIG. 12. The exclusion significance vs required luminosity at 27-TeV collider by projecting the distributions at 14-TeV collider to 27-TeV collider. The mass of the leptoquark has been taken to be $M_{LQ} = 1300$ GeV.

B. Log-likelihood ratio test

In this section, we study the prospect of distinguishing two models, if in the future, a scalar leptoquark of mass 1300 GeV is observed. It will take around 1600 fb^{-1} of data for a 5σ discovery. At this mass, for $\mathcal{L} = 3000$ fb^{-1}, with the optimized cuts chosen by BDT, the number of signal and background events are found to be (102, 145) for the S_3 model and (121, 170) for the R_2 model.[18] For these numbers of events we find the distribution of events with respect to $\frac{E_b}{E_t}$. We use log-likelihood ratio (LLR) hypothesis test for distinguishing two models.[19] The likelihood function is given by the product of Poisson distribution functions at all bins. That is, for O_i being the observed data and E_i being the expected data, the likelihood function $\mathcal{L}$ is given as

$$L(\mathrm{E}|\mathrm{O}) = \prod_{i=1}^{n} e^{-E_i} {E_i}^{O_i}/\Gamma(O_i + 1). \tag{5.5}$$

The exclusion significance of a model M1, when another model M2 is observed, is given as

$$Z_{M1|M2} = \sqrt{-2ln\frac{\mathcal{L}(\mathrm{M1}|\mathrm{M2})}{\mathcal{L}(\mathrm{M2}|\mathrm{M2})}}. \tag{5.6}$$

We have considered both the scenarios when either of the models is observed and the other one is predicted for which

TABLE IX. Probability of excluding one model when the other model is the observed model at 14-TeV LHC and 27-TeV HE-LHC with $\mathcal{L} = 3$ ab^{-1}.

$\mathcal{L}$	Predicted	Observed	Rejection probability (Z) (14 TeV)	Rejection probability (Z) (27 TeV)
3 ab^{-1}	$R_2 + B$	$S_3 + B$	0.98σ	6.45σ
	$S_3 + B$	$R_2 + B$	1.01σ	6.59σ

[18]Multiplying luminosity with the cross sections given in Table VI gives these event numbers.

[19]We have also checked with χ^2 hypothesis test and got similar kind of results.

we want to find the exclusion significance. To find distribution for event numbers for the predicted model, the signal events of it are scanned through the same BDT model used for the observed model. In Fig. 11, we show $\frac{E_b}{E_t}$ distribution for event numbers for observed and predicted models at 14-TeV LHC with 3 ab^{-1} of data. For the analysis, we have taken the first eight bins, starting from the left, of the $\frac{E_b}{E_t}$ distribution,[20] given in Fig. 11. We obtain an exclusion significance (Z) of 0.98σ, when $S3+B$ is taken as observed at the LHC and $R2+B$ is considered as the predicted one. For the reverse case, we obtain Z value as 1.01σ; see Table IX. As the exclusion significance is quite low, it shows that two models cannot be distinguished well at the LHC. However, it is interesting to see whether these two models can be distinguished at 27-TeV (HE-LHC) collider for the same mass of the leptoquark. To do this study, we assume that the shape of the signal and individual background distributions will remain the same at the 27-TeV LHC as that of the 14-TeV collider. We then scale the distributions by overall factors after calculating their total cross sections at these two different center-of-mass energy colliders. In Fig. 12, we show the plot for exclusion significance vs required luminosity at the HE-LHC. We find that with a moderate amount of luminosity (around 1800 fb^{-1}) at this collider, either of the models can be excluded at 5σ significance when the other one appears as observed. In the last column of Table IX, we show the exclusion significances for 3 ab^{-1} data at this collider.

VI. CONCLUSIONS

TeV-scale leptoquarks that can emerge from various models are well motivated and phenomenologically interesting to be searched at high-energy collider experiments. Present work investigates the pair production of third-generation $\frac{2}{3}e$-charged scalar leptoquark at the LHC using the NLO QCD accuracy, matched to parton shower for precise probing. Among different potential scalar leptoquark models, two primary interests, S_3 and R_2, can be probed by looking at their decay into a top with a tau neutrino, thus producing a compelling signature of a pair of toplike fatjets along with substantial missing transverse energy. Here tops, created from heavy leptoquarks, are naturally boosted and therefore considering them as boosted jets is quite meaningful.

With a precise understanding of jet physics, it is now possible to study the intrinsic substructure and properties of such jets, thereby pointing out the origin of these jets with a high degree of accuracy. Therefore, the considered channel has excellent potential for separating the tiny signal from the overwhelming SM background. Parton shower effects are included in our study and its usefulness in the low transverse momentum region is seen in Fig. 2. We also demonstrate that the factorization and renormalization-scale uncertainties for the NLO + PS events are much lower than that of LO + PS events (see Fig. 4 and Table II).

For accurate prediction, we include all the relevant background processes with two to four extra QCD radiations and normalize them using the available higher-order QCD-corrected production cross-section. Different high-level variables, such as MET, M_{eff}, $\Delta R(J_0, J_1)$, $\Delta\phi(J_i, \not{E}_T)$, jet substructure-based pruned jet mass, and N-subjettiness are proved to be efficacious to pinpoint the signal. Multivariate analysis is carried out individually for these two models and we show that at the 14-TeV LHC with an integrated luminosity of 3000 fb^{-1}, the leptoquarks of mass 1380 GeV can be discovered (5σ), and up to 1520 GeV can be excluded (2σ).

Among the two scalar leptoquark models considered here, it is interesting to note that the top quarks resulting from the decay of leptoquarks possess different helicities. Most of the high-level variables utilized for multivariate analysis are not sensitive to this polarization. Only the jet mass variables acquire some minor effect due to the modified distribution pattern in the decay process. However, these are insignificant enough, thereby providing almost equivalent mass constraints for both models.

We further construct different polarization-sensitive variables to distinguish these scalar leptoquark models of the same charge. We exhibit the effectiveness of such variables in terms of (i) an angular variable in the top quark's rest frame, and (ii) the ratio of the energy variables $\frac{E_b}{E_t}$. Such effects are demonstrated at the truth level and after including parton shower and (fat)jet formation (see Figs. 9 and 10). Significant distortion is noticeable following detector simulation and (fat)jet formation. This is primarily attributed to the contamination and poor measurement efficiency of the b-jet momenta within a highly collimated toplike fatjet. The LLR hypothesis test is used to distinguish the models in the presence of combined background events. We find that the statistical exclusion significance remains low at around 1σ confidence level at the LHC. However, it is shown that the 27-TeV collider can play a promising role and it is estimated that the required luminosity would be around 300 fb^{-1} (1800 fb^{-1}) to distinguish these two models with 2σ (5σ) significance.

ACKNOWLEDGMENTS

We thank Rinku Maji and Saurabh K. Shukla for fruitful discussions. Computational works are performed using the High Performance Computing resources (Param Vikram-1000) and the TDP project equipment at PRL.

[20]For the bins around $z = 0.8$ and above, the b-jet energy is not very well measured. In this region, because of very high boost of top quark, b jet gets contaminated with the other two light jets, originated from the hadronic decay of top quark.

APPENDIX

1. Distribution of daughter of top quark

Here, we will find the differential distribution of decay width of right-handed top in its rest frame. The distribution for left-handed particle can be obtained similarly.

The Feynman diagram for top decay is shown in Fig. 13 and the matrix element can be written as

$$M = \bar{u}_b(p_1)\frac{ig}{\sqrt{2}}\gamma_\mu P_L u_t(m_t)\epsilon^{\mu*}_{W^+}(p_2). \tag{A1}$$

So, $|M|^2$ can be written as

$$|M|^2 = \frac{g^2}{2}\bar{u}_b(p_1)\gamma_\mu P_L u_t(m_t)\bar{u}_t(m_t)P_R\gamma_\nu u_b(p_1)\epsilon^{\mu*}_{W^+}(p_2)\epsilon^{\nu}_{W^+}(p_2)$$
$$\sum_{\text{final spins}}|M|^2 = -\frac{g^2}{2}\mathrm{Tr}[\gamma_\mu P_L u_t(m_t)\bar{u}_t(m_t)P_R\gamma_\nu(\not{p}1 + m_b)]\left(g^{\mu\nu} - \frac{p^\mu p^\nu}{M_W^2}\right). \tag{A2}$$

In the Weyl basis, $\gamma^\mu = \left(\begin{smallmatrix}0 & \sigma^\mu\\ \bar{\sigma}^\mu & 0\end{smallmatrix}\right)$ and $\gamma^5 = \left(\begin{smallmatrix}-I & 0\\ 0 & I\end{smallmatrix}\right)$, where $\sigma^\mu = (I, \boldsymbol{\sigma})$ and $\bar{\sigma}^\mu = (I, -\boldsymbol{\sigma})$. The spinor in the rest frame is given by

$$u_t^s(m_t) = \sqrt{m_t}\begin{pmatrix}\xi^s\\ \xi^s\end{pmatrix}.$$

Using the above expressions, Eq. (A2) can be written as

$$\sum_{\text{final spins}}|M|^2 = -\frac{g^2 m_t}{2}\mathrm{Tr}\left[\begin{pmatrix}0 & 0\\ \bar{\sigma}_\mu & 0\end{pmatrix}\begin{pmatrix}\xi^s\xi^{s\dagger} & \xi^s\xi^{s\dagger}\\ \xi^s\xi^{s\dagger} & \xi^s\xi^{s\dagger}\end{pmatrix}\begin{pmatrix}0 & 0\\ \bar{\sigma}_\nu & 0\end{pmatrix}\not{p}1\right]\left(g^{\mu\nu} - \frac{p^\mu p^\nu}{M_W^2}\right)$$
$$= -\frac{g^2 m_t}{2}\mathrm{Tr}\left[\bar{\sigma}^\mu\xi^s\xi^{s\dagger}\bar{\sigma}_\mu\sigma\cdot p_1 - \frac{\bar{\sigma}\cdot p_2\xi^s\xi^{s\dagger}\bar{\sigma}\cdot p_2\sigma\cdot p_1}{M_W^2}\right]. \tag{A3}$$

For the spin-up top $\xi^s\xi^{s\dagger}$ can be written as $\frac{I+\sigma^3}{2}$. So, Eq. (A3) can be written as

$$\sum_{\text{final spins}}|M|^2 = -\frac{g^2 m_t}{4}\mathrm{Tr}\left[\bar{\sigma}^\mu(I+\sigma^3)\bar{\sigma}_\mu\sigma\cdot p_1 - \frac{\bar{\sigma}\cdot p_2(I+\sigma^3)\bar{\sigma}\cdot p_2\sigma\cdot p_1}{M_W^2}\right]. \tag{A4}$$

Using $\sigma^i\sigma^j + \sigma^j\sigma^i = 2\delta^{ij}I$, the following can be proven:

$$\bar{\sigma}^\mu\bar{\sigma}_\mu = -2I, \tag{A5}$$

$$\bar{\sigma}^\mu\sigma^3\bar{\sigma}_\mu = 2\sigma^3, \tag{A6}$$

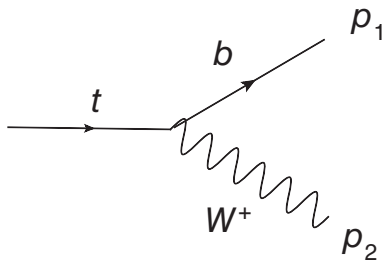

FIG. 13. The Feynman diagram for top decay.

$$\bar{\sigma}\cdot p_2\bar{\sigma}\cdot p_2 = (p_2^0)^2 I + \vec{p_2}^2 I + 2\sigma^i p_2^i p_2^0, \tag{A7}$$

$$\bar{\sigma}\cdot p_2\sigma^3\bar{\sigma}\cdot p_2 = (p_2^0)^2\sigma^3 + 2p_2^3 p_2^0 I - \sigma^3\vec{p_2}^2 + 2\sigma^i p_2^3 p_2^i. \tag{A8}$$

Again, the following relations can be proven easily:

$$\mathrm{Tr}(\sigma^i\sigma^j) = 2\delta^{ij}, \tag{A9}$$

$$\mathrm{Tr}(\sigma^i) = 0, \tag{A10}$$

$$\mathrm{Tr}(\sigma\cdot a) = 2a^0. \tag{A11}$$

The different parts of Eq. (A4) can be obtained using Eqs. (A5)–(A11). After using them, we have

$$\mathrm{Tr}[\bar{\sigma}^{\mu}\bar{\sigma}_{\mu}\sigma\cdot p_1] = -4p_1^0, \tag{A12}$$

$$\mathrm{Tr}[\bar{\sigma}^{\mu}\sigma^3\bar{\sigma}_{\mu}\sigma\cdot p_1] = -4p_1^3, \tag{A13}$$

$$\mathrm{Tr}[\bar{\sigma}\cdot p_2\bar{\sigma}\cdot p_2\sigma\cdot p_1] = 2p_1^0(p_2^0)^2 + 2p_1^0\vec{p}_2{}^2 - 4\vec{p}_1\cdot\vec{p}_2p_2^0, \tag{A14}$$

$$\mathrm{Tr}[\bar{\sigma}\cdot p_2\sigma^3\bar{\sigma}\cdot p_2\sigma\cdot p_1] = -2(p_2^0)^2p_1^3 + 4p_2^3p_2^0p_1^0 + 2p_1^3\vec{p}_2{}^2 - 4p_2^3\vec{p}_1\cdot\vec{p}_2. \tag{A15}$$

Using energy conservation in the top rest frame,

$$m_t = |\vec{p}_1| + \sqrt{\vec{p}_1{}^2 + m_W^2},$$
$$|\vec{p}_1| = \frac{m_t^2 - m_W^2}{2m_t}. \tag{A16}$$

Equation (A14) can be written as

$$\begin{aligned} &2p_1^0(p_2^0)^2 + 2p_1^0\vec{p}_2{}^2 - 4\vec{p}_1\cdot\vec{p}_2p_2^0 \\ &= 2p_1^0(m_W^2 + 2\vec{p}_1{}^2) + 4\vec{p}_1\cdot\vec{p}_1(m_t - p_1^0) \\ &= 2|\vec{p}_1|(m_W^2 + 2|\vec{p}_1|m_t) = 2|\vec{p}_1|m_t.{}^2 \end{aligned} \tag{A17}$$

Equation (A15) can be written as

$$\begin{aligned} &-2(p_2^0)^2p_1^3 + 4p_2^3p_2^0p_1^0 + 2p_1^3\vec{p}_2{}^2 - 4p_2^3\vec{p}_1\cdot\vec{p}_2 \\ &= -2p_1^3((p_2^0)^2 - \vec{p}_2{}^2) + 4p_2^3(p_2^0p_1^0 - \vec{p}_1\cdot\vec{p}_2) \\ &= -2p_1^3(m_W^2) - 2p_1^3(m_t^2 - m_W^2) = -2p_1^3m_t^2. \end{aligned} \tag{A18}$$

Using the above formulas in Eq. (A4), we have

$$\begin{aligned} \sum_{\text{final spins}}|M|^2 &= -\frac{g^2m_t}{4}\left[-4p_1^0 - 4p_1^3 - \frac{2|\vec{p}_1|m_t^2 - 2p_1^3m_t^2}{M_W^2}\right] \\ &= g^2m_t\left[\left(1+\frac{m_t^2}{2M_W^2}\right) + \left(1-\frac{m_t^2}{2M_W^2}\right)\cos\theta_b\right] \\ &= g^2m_t\left(1+\frac{m_t^2}{2M_W^2}\right)\left[1+\frac{2M_W^2 - m_t^2}{2M_W^2 + m_t^2}\cos\theta_b\right] \\ &= g^2m_t\left(1+\frac{m_t^2}{2M_W^2}\right)[1 + k_b\cos\theta_b], \end{aligned}$$

where $k_b = \frac{2M_W^2 - m_t^2}{2M_W^2 + m_t^2} = -0.4$, spin-analyzing power of b quark.

The differential distribution of decay width for right-handed top quark is given by

$$\begin{aligned} \frac{d\Gamma}{d\cos\theta_b} &= \frac{1}{2m_t^2}\frac{|\vec{p}_1|}{8\pi}\sum_{\text{final spins}}|M|^2 \\ &= \frac{1}{2m_t^2}\frac{1}{8\pi}\frac{m_t^2 - m_W^2}{2m_t}g^2m_t\left(1+\frac{m_t^2}{2M_W^2}\right) \\ &\quad\times[1 + k_b\cos\theta_b] \\ &= \frac{g^2}{32\pi}\frac{(m_t^2 - m_W^2)(2M_W^2 + m_t^2)}{m_t^2m_W^2}[1 + k_b\cos\theta_b]. \end{aligned}$$

For the spin-down top, $\xi^s\xi^{s\dagger}$ can be written as $\frac{I-\sigma^3}{2}$. So, it is easy follow that in the above expression there will be a minus sign in front of k_b for this case.

2. Relation between $\cos\theta_b'$ and z

In the following, quantities in the lab frame will be denoted by unprimed symbols, whereas in the top rest frame they will be denoted by primed symbols.[21] So, in the rest frame of the top quark the angle of the bottom quark's direction of motion with the boost direction of the top quark is given by

$$\cos\theta_b' = \frac{p_b^{z'}}{|\vec{p}_b{}'|}, \tag{A19}$$

where z and z' axes are along the direction of motion of the top quark in the lab frame.

Using Lorentz transformation between two frames with $\beta = \frac{|\vec{p}_t|}{E_t}$ and $\gamma = \frac{1}{\sqrt{1-\beta^2}} = \frac{E_t}{m_t}$,

$$p_b^{z'} = -\gamma\beta E_b + \gamma p_b^z. \tag{A20}$$

Using energy conservation in the lab frame,

$$\begin{aligned} E_t &= E_b + \sqrt{(\vec{p}_t - \vec{p}_b)^2 + m_W^2} \\ p_b^z &= -\frac{m_t^2 + m_b^2 - m_W^2 - 2E_tE_b}{2|\vec{p}_t|} \\ &= \frac{E_b}{\beta} - \frac{m_t^2 + m_b^2 - m_W^2}{2\beta\gamma m_t}. \end{aligned} \tag{A21}$$

[21]Note in the main text we did not use any prime for the angle in the rest frame. So, the $\cos\theta_b'$ here is the same as $\cos\theta_b$ in the main text.

Using Eq. (A21) in Eq. (A20), we have

$$\begin{aligned} p_b^{z'} &= -\gamma\beta E_b + \gamma\frac{E_b}{\beta} - \frac{m_t^2 + m_b^2 - m_W^2}{2\beta m_t} \\ &= \frac{zE_t}{\gamma\beta} - \frac{m_t^2 + m_b^2 - m_W^2}{2\beta m_t} \\ &= \frac{zm_t}{\beta} - \frac{m_t^2 + m_b^2 - m_W^2}{2\beta m_t}. \end{aligned}$$

Assuming $m_b = 0$,

$$p_b^{z'} = \frac{1}{\beta}\left(zm_t - \frac{m_t^2 - m_W^2}{2m_t}\right). \tag{A22}$$

Using energy conservation in the top rest frame,

$$\begin{aligned} m_t &= E_b' + \sqrt{\vec{p}_b'^2 + m_W^2}, \\ |\vec{p}_b'| &= \frac{m_t^2 - m_W^2}{2m_t}. \end{aligned} \tag{A23}$$

Using Eqs. (A22) and (A23) in Eq. (A19), we have

$$\cos\theta_b' = \frac{1}{\beta}\left(\frac{2m_t^2}{m_t^2 - m_W^2}z - 1\right). \tag{A24}$$

[1] J. C. Pati and A. Salam, Lepton number as the fourth color, Phys. Rev. D **10**, 275 (1974).
[2] J. C. Pati and A. Salam, Unified lepton-hadron symmetry and a gauge theory of the basic interactions, Phys. Rev. D **8**, 1240 (1973).
[3] H. Georgi and S. L. Glashow, Unity of All Elementary Particle Forces, Phys. Rev. Lett. **32**, 438 (1974).
[4] P. Langacker, Grand unified theories and proton decay, Phys. Rep. **72**, 185 (1981).
[5] J. Wudka, Composite leptoquarks, Phys. Lett. **167B**, 337 (1986).
[6] W. Buchmuller, R. Ruckl, and D. Wyler, Leptoquarks in lepton—quark collisions, Phys. Lett. B **191**, 442 (1987).
[7] *BABAR* Collaboration, Measurement of an excess of $\bar{B} \to D^{(*)}\tau^-\bar{\nu}_\tau$ decays and implications for charged Higgs bosons, Phys. Rev. D **88**, 072012 (2013).
[8] BELLE Collaboration, Test of lepton flavor universality and search for lepton flavor violation in $B \to K\ell\ell$ decays, J. High Energy Phys. 03 (2021) 105.
[9] Belle Collaboration, Measurement of $\mathcal{R}(D)$ and $\mathcal{R}(D^*)$ with a semileptonic tagging method, arXiv:1904.08794.
[10] Belle Collaboration, Test of Lepton-Flavor Universality in $B \to K^*\ell^+\ell^-$ Decays at Belle, Phys. Rev. Lett. **126**, 161801 (2021).
[11] LHCb Collaboration, Measurement of the Ratio of Branching Fractions $\mathcal{B}(\bar{B}^0 \to D^{*+}\tau^-\bar{\nu}_\tau)/\mathcal{B}(\bar{B}^0 \to D^{*+}\mu^-\bar{\nu}_\mu)$, Phys. Rev. Lett. **115**, 111803 (2015).
[12] LHCb Collaboration, Measurement of the ratios of branching fractions $\mathcal{R}(D^*)$ and $\mathcal{R}(D^0)$, arXiv:2302.02886.
[13] LHCb Collaboration, Measurement of lepton universality parameters in $B^+ \to K^+\ell^+\ell^-$ and $B^0 \to K^{*0}\ell^+\ell^-$ decays, arXiv:2212.09153.
[14] LHCb Collaboration, Test of lepton universality in $b \to s\ell^+\ell^-$ decays, arXiv:2212.09152.
[15] N. Desai and A. Sengupta, Status of leptoquark models after LHC Run-2 and discovery prospects at future colliders, arXiv:2301.01754.
[16] ATLAS Collaboration, Search for pairs of scalar leptoquarks decaying into quarks and electrons or muons in $\sqrt{s} =$ 13 TeV pp collisions with the ATLAS detector, J. High Energy Phys. 10 (2020) 112.
[17] ATLAS Collaboration, Search for pair-produced scalar and vector leptoquarks decaying into third-generation quarks and first- or second-generation leptons in pp collisions with the ATLAS detector, J. High Energy Phys. 06 (2023) 188.
[18] ATLAS Collaboration, Searches for scalar leptoquarks and differential cross-section measurements in dilepton-dijet events in proton-proton collisions at a centre-of-mass energy of $\sqrt{s} = 13$ TeV with the ATLAS experiment, Eur. Phys. J. C **79**, 733 (2019).
[19] CMS Collaboration, Search for pair production of second-generation leptoquarks at $\sqrt{s} = 13$ TeV, Phys. Rev. D **99**, 032014 (2019).
[20] CMS Collaboration, Search for pair production of first-generation scalar leptoquarks at $\sqrt{s} = 13$ TeV, Phys. Rev. D **99**, 052002 (2019).
[21] ATLAS Collaboration, Search for pair production of third-generation leptoquarks decaying into a bottom quark and a τ-lepton with the ATLAS detector, arXiv:2303.01294.
[22] CMS Collaboration, Search for singly and pair-produced leptoquarks coupling to third-generation fermions in proton-proton collisions at $s = 13$ TeV, Phys. Lett. B **819**, 136446 (2021).
[23] CMS Collaboration, Constraints on models of scalar and vector leptoquarks decaying to a quark and a neutrino at $\sqrt{s} = 13$ TeV, Phys. Rev. D **98**, 032005 (2018).
[24] B. Gripaios, A. Papaefstathiou, K. Sakurai, and B. Webber, Searching for third-generation composite leptoquarks at the LHC, J. High Energy Phys. 01 (2011) 156.

[25] K. Chandak, T. Mandal, and S. Mitra, Hunting for scalar leptoquarks with boosted tops and light leptons, Phys. Rev. D **100**, 075019 (2019).
[26] A. Bhaskar, T. Mandal, S. Mitra, and M. Sharma, Improving third-generation leptoquark searches with combined signals and boosted top quarks, Phys. Rev. D **104**, 075037 (2021).
[27] G. Belanger *et al.*, Leptoquark manoeuvres in the dark: A simultaneous solution of the dark matter problem and the $R_{D^{(*)}}$ anomalies, J. High Energy Phys. 02 (2022) 042.
[28] ATLAS Collaboration, Searches for third-generation scalar leptoquarks in $\sqrt{s} = 13$ TeV pp collisions with the ATLAS detector, J. High Energy Phys. 06 (2019) 144.
[29] CMS Collaboration, The search for a third-generation leptoquark coupling to a τ lepton and a b quark through single, pair and nonresonant production at $\sqrt{s} = 13$ TeV, Report No. CMS-PAS-EXO-19-016, 2022.
[30] ATLAS Collaboration, Search for a scalar partner of the top quark in the all-hadronic $t\bar{t}$ plus missing transverse momentum final state at $\sqrt{s} = 13$ TeV with the ATLAS detector, Eur. Phys. J. C **80**, 737 (2020).
[31] N. Vignaroli, Seeking leptoquarks in the $t\bar{t}$ plus missing energy channel at the high-luminosity LHC, Phys. Rev. D **99**, 035021 (2019).
[32] P. Bandyopadhyay, S. Dutta, M. Jakkapu, and A. Karan, Distinguishing leptoquarks at the LHC/FCC, Nucl. Phys. **B971**, 115524 (2021).
[33] V. D. Barger, J. Ohnemus, and R. J. N. Phillips, Spin correlation effects in the hadroproduction and decay of very heavy top quark pairs, Int. J. Mod. Phys. A **04**, 617 (1989).
[34] K. Hagiwara and D. Zeppenfeld, Helicity amplitudes for heavy lepton production in e^+e^- annihilation, Nucl. Phys. **B274**, 1 (1986).
[35] G. L. Kane, G. A. Ladinsky, and C. P. Yuan, Using the top quark for testing Standard Model polarization and *CP* predictions, Phys. Rev. D **45**, 124 (1992).
[36] R. H. Dalitz and G. R. Goldstein, The decay and polarization properties of the top quark, Phys. Rev. D **45**, 1531 (1992).
[37] Y. Sumino and S. Tsuno, New method for reconstructing effective top quark spin, Phys. Lett. B **633**, 715 (2006).
[38] R. M. Godbole, S. D. Rindani, and R. K. Singh, Lepton distribution as a probe of new physics in production and decay of the t quark and its polarization, J. High Energy Phys. 12 (2006) 021.
[39] W. Bernreuther, Top quark physics at the LHC, J. Phys. G **35**, 083001 (2008).
[40] J. Shelton, Polarized tops from new physics: Signals and observables, Phys. Rev. D **79**, 014032 (2009).
[41] R. M. Godbole, S. D. Rindani, K. Rao, and R. K. Singh, Top polarization as a probe of new physics, AIP Conf. Proc. **1200**, 682 (2010).
[42] R. M. Godbole, K. Rao, S. D. Rindani, and R. K. Singh, On measurement of top polarization as a probe of $t\bar{t}$ production mechanisms at the LHC, J. High Energy Phys. 11 (2010) 144.
[43] B. Bhattacherjee, S. K. Mandal, and M. Nojiri, Top polarization and stop mixing from boosted jet substructure, J. High Energy Phys. 03 (2013) 105.
[44] W. Bernreuther, P. González, and C. Mellein, Decays of polarized top quarks to lepton, neutrino and jets at NLO QCD, Eur. Phys. J. C **74**, 2815 (2014).
[45] V. A. Prasath, R. M. Godbole, and S. D. Rindani, Longitudinal top polarisation measurement and anomalous Wtb coupling, Eur. Phys. J. C **75**, 402 (2015).
[46] S. Bhattacharya, M. Guchait, and A. H. Vijay, Boosted top quark tagging and polarization measurement using machine learning, Phys. Rev. D **105**, 042005 (2022).
[47] D. Krohn, J. Shelton, and L.-T. Wang, Measuring the polarization of boosted hadronic tops, J. High Energy Phys. 07 (2010) 041.
[48] A. Papaefstathiou and K. Sakurai, Determining the helicity structure of third generation resonances, J. High Energy Phys. 06 (2012) 069.
[49] J. Roy, Probing leptoquark chirality via top polarization at the colliders, arXiv:1811.12058.
[50] R. Allahverdi, M. Dalchenko, B. Dutta, A. Flórez, Y. Gao, T. Kamon, N. Kolev, R. Mueller, and M. Segura, Distinguishing standard model extensions using monotop chirality at the LHC, J. High Energy Phys. 12 (2016) 046.
[51] M. Kramer, T. Plehn, M. Spira, and P. M. Zerwas, Pair production of scalar leptoquarks at the CERN LHC, Phys. Rev. D **71**, 057503 (2005).
[52] T. Mandal, S. Mitra, and S. Seth, Pair production of scalar leptoquarks at the LHC to NLO parton shower accuracy, Phys. Rev. D **93**, 035018 (2016).
[53] I. Doršner, S. Fajfer, A. Greljo, J. F. Kamenik, and N. Košnik, Physics of leptoquarks in precision experiments and at particle colliders, Phys. Rep. **641**, 1 (2016).
[54] D. Binosi and L. Theussl, JaxoDraw: A graphical user interface for drawing Feynman diagrams, Comput. Phys. Commun. **161**, 76 (2004).
[55] J. Alwall, R. Frederix, S. Frixione, V. Hirschi, F. Maltoni, O. Mattelaer, H.-S. Shao, T. Stelzer, P. Torrielli, and M. Zaro, The automated computation of tree-level and next-to-leading order differential cross sections, and their matching to parton shower simulations, J. High Energy Phys. 07 (2014) 079.
[56] A. Alloul, N. D. Christensen, C. Degrande, C. Duhr, and B. Fuks, FeynRules 2.0—A complete toolbox for tree-level phenomenology, Comput. Phys. Commun. **185**, 2250 (2014).
[57] C. Degrande, Automatic evaluation of UV and R2 terms for beyond the standard model Lagrangians: A proof-of-principle, Comput. Phys. Commun. **197**, 239 (2015).
[58] G. Ossola, C. G. Papadopoulos, and R. Pittau, Reducing full one-loop amplitudes to scalar integrals at the integrand level, Nucl. Phys. **B763**, 147 (2007).
[59] C. Degrande, C. Duhr, B. Fuks, D. Grellscheid, O. Mattelaer, and T. Reiter, UFO—The universal FeynRules output, Comput. Phys. Commun. **183**, 1201 (2012).
[60] S. Frixione, Z. Kunszt, and A. Signer, Three jet cross-sections to next-to-leading order, Nucl. Phys. **B467**, 399 (1996).
[61] S. Frixione, A general approach to jet cross-sections in QCD, Nucl. Phys. **B507**, 295 (1997).
[62] S. Frixione and B. R. Webber, Matching NLO QCD computations and parton shower simulations, J. High Energy Phys. 06 (2002) 029.

[63] C. Bierlich *et al.*, A comprehensive guide to the physics and usage of PYTHIA 8.3, arXiv:2203.11601.
[64] A. Ghosh, P. Konar, and S. Seth, Precise probing of the inert Higgs-doublet model at the LHC, Phys. Rev. D **105**, 115038 (2022).
[65] A. Ghosh, P. Konar, and R. Roshan, Top-philic dark matter in a hybrid KSVZ axion framework, J. High Energy Phys. 12 (2022) 167.
[66] M. L. Mangano, M. Moretti, F. Piccinini, and M. Treccani, Matching matrix elements and shower evolution for top-quark production in hadronic collisions, J. High Energy Phys. 01 (2007) 013.
[67] S. Hoeche, F. Krauss, N. Lavesson, L. Lonnblad, M. Mangano, A. Schalicke *et al.*, Matching parton showers and matrix elements, in *HERA and the LHC: A Workshop on the Implications of HERA for LHC Physics: CERN—DESY Workshop 2004/2005 (Midterm Meeting, CERN, 2004; Final Meeting, DESY, 2005)* (2005), pp. 288–289, 10.5170/CERN-2005-014.288.
[68] DELPHES 3 Collaboration, DELPHES 3, A modular framework for fast simulation of a generic collider experiment, J. High Energy Phys. 02 (2014) 057.
[69] Y. L. Dokshitzer, G. D. Leder, S. Moretti, and B. R. Webber, Better jet clustering algorithms, J. High Energy Phys. 08 (1997) 001.
[70] M. Cacciari, G. P. Salam, and G. Soyez, FastJet user manual, Eur. Phys. J. C **72**, 1896 (2012).
[71] C. Muselli, M. Bonvini, S. Forte, S. Marzani, and G. Ridolfi, Top quark pair production beyond NNLO, J. High Energy Phys. 08 (2015) 076.
[72] N. Kidonakis, Theoretical results for electroweak-boson and single-top production, Proc. Sci. DIS2015 (**2015**) 170 [arXiv:1506.04072].
[73] S. Catani, L. Cieri, G. Ferrera, D. de Florian, and M. Grazzini, Vector Boson Production at Hadron Colliders: A Fully Exclusive QCD Calculation at NNLO, Phys. Rev. Lett. **103**, 082001 (2009).
[74] G. Balossini, G. Montagna, C. M. Carloni Calame, M. Moretti, O. Nicrosini, F. Piccinini, M. Treccani, and A. Vicini, Combination of electroweak and QCD corrections to single W production at the Fermilab Tevatron and the CERN LHC, J. High Energy Phys. 01 (2010) 013.
[75] J. M. Campbell, R. K. Ellis, and C. Williams, Vector boson pair production at the LHC, J. High Energy Phys. 07 (2011) 018.
[76] D. Krohn, J. Thaler, and L.-T. Wang, Jet trimming, J. High Energy Phys. 02 (2010) 084.
[77] J. M. Butterworth, A. R. Davison, M. Rubin, and G. P. Salam, Jet Substructure as a New Higgs Search Channel at the LHC, Phys. Rev. Lett. **100**, 242001 (2008).
[78] S. D. Ellis, C. K. Vermilion, and J. R. Walsh, Techniques for improved heavy particle searches with jet substructure, Phys. Rev. D **80**, 051501 (2009).
[79] S. D. Ellis, C. K. Vermilion, and J. R. Walsh, Recombination algorithms and jet substructure: Pruning as a tool for heavy particle searches, Phys. Rev. D **81**, 094023 (2010).
[80] J. Thaler and K. Van Tilburg, Identifying boosted objects with N-subjettiness, J. High Energy Phys. 03 (2011) 015.
[81] J. Thaler and K. Van Tilburg, Maximizing boosted top identification by minimizing N-subjettiness, J. High Energy Phys. 02 (2012) 093.
[82] P. Konar, K. Kong, and K. T. Matchev, $\sqrt{\hat{s}}_{\mathrm{min}}$: A global inclusive variable for determining the mass scale of new physics in events with missing energy at hadron colliders, J. High Energy Phys. 03 (2009) 085.
[83] C. G. Lester and D. J. Summers, Measuring masses of semiinvisibly decaying particles pair produced at hadron colliders, Phys. Lett. B **463**, 99 (1999).
[84] A. J. Barr, T. J. Khoo, P. Konar, K. Kong, C. G. Lester, K. T. Matchev, and M. Park, Guide to transverse projections and mass-constraining variables, Phys. Rev. D **84**, 095031 (2011).
[85] A. Hocker *et al.*, TMVA—Toolkit for multivariate data analysis, arXiv:physics/0703039.
[86] A. Czarnecki, J. G. Korner, and J. H. Piclum, Helicity fractions of W bosons from top quark decays at NNLO in QCD, Phys. Rev. D **81**, 111503 (2010).
[87] ATLAS Collaboration, Measurement of the W boson polarization in top quark decays with the ATLAS detector, J. High Energy Phys. 06 (2012) 088.